

Mathematical Models and Methods in Applied Sciences
© World Scientific Publishing Company

Accurate numerical simulation of electrodiffusion and water movement in brain tissue

Ada Johanne Ellingsrud

Simula Research Laboratory, Oslo, Norway.
ada@simula.no

Nicolas Boullé

Mathematical Institute, University of Oxford, Oxford, UK.
boulle@maths.ox.ac.uk

Patrick E. Farrell

Mathematical Institute, University of Oxford, Oxford, UK.
patrick.farrell@maths.ox.ac.uk

Marie E. Rognes

Simula Research Laboratory, Oslo, Norway.
meg@simula.no

Mathematical modelling of ionic electrodiffusion and water movement is emerging as a powerful avenue of investigation to provide new physiological insight into brain homeostasis. However, in order to provide solid answers and resolve controversies, the accuracy of the predictions is essential. Ionic electrodiffusion models typically comprise non-trivial systems of non-linear and highly coupled partial and ordinary differential equations that govern phenomena on disparate time scales. Here, we study numerical challenges related to approximating these systems. We consider a homogenized model for electrodiffusion and osmosis in brain tissue and present and evaluate different associated finite element-based splitting schemes in terms of their numerical properties, including accuracy, convergence, and computational efficiency for both idealized scenarios and for the physiologically relevant setting of cortical spreading depression (CSD). We find that the schemes display optimal convergence rates in space for problems with smooth manufactured solutions. However, the physiological CSD setting is challenging: we find that the accurate computation of CSD wave characteristics (wave speed and wave width) requires a very fine spatial and fine temporal resolution.

Keywords: electrodiffusion, osmosis, brain electrophysiology and mechanics, finite element method, splitting scheme, numerical convergence

AMS Subject Classification: 22E46, 53C35, 57S20

2 *A. J. Ellingsrud, N. Boullé, P. E. Farrell, and M. E. Rognes*

1. Introduction

The movement of ions and molecules in and between cellular compartments is fundamental for brain function, and importantly for neuronal excitability and activity^{1,25,47}. Vital processes such as action potential firing, transmitter release, and synaptic transmission are all driven by ionic gradients across the neuronal membrane. Regulation of the extracellular volume by cellular swelling is closely related to ionic dynamics, including potassium buffering^{16,21}. Concurrently, several pathologies are associated with disruption to ionic homeostasis in the brain, e.g. Huntington's disease⁴¹, multiple sclerosis³⁶, migraine³⁷, epilepsy²⁰, Alzheimer's disease²⁶, and cortical spreading depression³¹. Recent research efforts indicate that ion concentrations in the extracellular space are not static, but vary across states such as locomotion² and the sleep cycle⁵.

In spite of these aspects, mathematical and numerical models for describing dynamics in brain tissue traditionally assume that the ion concentrations are constant in time and space. Although such models have provided valuable insight into the mechanisms underlying excitable cells, they fail to represent essential dynamics related to altered ion concentrations in brain tissue. Recently, several mathematical models also including electrodiffusive effects have been presented^{4,10,15,18,19,24,30,32,34,35,46}. However, to date little attention has been paid to the numerical solution of these models.

In this paper, we consider a mathematical framework proposed by Mori²⁴, consisting of a system of partial differential equations (PDEs) governing ionic electrodiffusion and water flow in biological tissue, coupled to a system of ordinary differential equations (ODEs) describing the temporal evolution of ionic membrane mechanisms. The system predicts the dynamics of volume fractions, ion concentrations, electrical potentials and mechanical pressure in an arbitrary number of cellular compartments and in the extracellular space (ECS). The cellular compartments can communicate with the ECS via transmembrane ion and water fluxes. This mathematical model extends on the celebrated bidomain model^{7,8,43}, and both represent the tissue in a homogenized manner. Homogenized models are coarse-grained, and hence well suited for simulating phenomena on the tissue scale (mm). Importantly, the two models differ in that the classical bidomain model only predicts electrical potentials, whereas the model for ionic electrodiffusion and water flow takes into account how the movement of ions affect the excitable tissue, both in terms of electrochemical and mechanical effects.

Previously, the electrodiffusive model (in its zero flow limit) has been used to study dynamics in brain tissue, and in particular cortical spreading depression (CSD)^{28,45}. CSD is a slowly propagating wave of depolarization of brain cells, characterized by elevated levels of extracellular potassium, calcium, and glutamate, cellular swelling and pronounced ECS shrinkage^{3,31}. Importantly, CSD is a fundamental pattern of brain signalling that challenges ionic homeostasis mechanisms in the brain. As such, a better understanding of the sequence of events in CSD has the

potential to provide new insight into underlying processes both in cerebral physiology and pathology¹¹. The aforementioned computational studies have focused on providing new insight into the role of glial cells in CSD²⁸, and the role of glutamate dynamics in CSD⁴⁵. However, in order to provide true physiological insight, the accuracy of the numerical and computational predictions is key; the difference between conflicting experimental observations may very well be within the numerical error of underresolved models.

Previously considered numerical schemes for the electrodiffusive model are based on finite difference^{24,28} or finite volume⁴⁵ discretizations in space and a backward Euler scheme (with explicit treatment of the active membrane flux) in time. The spatio-temporal discretization sizes of these schemes are reported to be on the order of $\Delta x \approx 0.02 - 0.2$ mm and $\Delta t \approx 10$ ms. By applying a (comparable) finite element scheme in space and a similar discretization scheme in time, we find that the CSD wave properties change substantially during spatial and temporal refinement. In particular, we observe that the wave speed and the width of the wave *increase* with decreasing time resolution, and *decrease* with decreasing spatial resolution (Figure 1). As the Mori framework comprises a system of non-linear and highly coupled partial and ordinary differential equations, governing phenomena on disparate time scales (both fast electrotonic effects and much slower effects mediated by diffusion), theoretical analysis of the full equations is challenging. In this paper, we take a natural first step towards accurate and efficient approximation schemes for the system by comparing different schemes numerically, with an emphasis on convergence and performance for simulating CSD waves.

In the first instance, we consider a low-order finite element scheme in space for the electrodiffusive model in the zero flow limit, and numerically study the effect of: (i) different operator splitting schemes, (ii) choice of time stepping schemes for the PDEs, (iii) choice of time stepping schemes for the ODEs, and (iv) a higher order spatial discretization scheme. All schemes display optimal convergence rates during refinement in space and time for problems with smooth manufactured solutions. However, we find that the accurate computation of CSD wave characteristics (such as wave speed and wave width) requires a very fine spatial and fine temporal resolution for all schemes tested. In particular, the different splitting schemes and PDE time stepping give comparable results in terms of accuracy. We observe that higher order ODE time stepping schemes (ESDIRK4, RK4) yield slightly faster convergence than the lower order backward Euler scheme. Finally, we find that applying a higher order finite element scheme with a coarser spatial resolution gives comparable results to the lower order finite element scheme in terms of accuracy, but at a higher cost, justifying the use of a low order scheme with fine spatial resolution.

We then turn to consider the full mathematical model, where the electrochemical and mechanical dynamics described in the zero flow limit are coupled with microscopic fluid dynamics. To the best of our knowledge, the only previous study involving this model was presented by O'Connell²⁷, studying the effects of mechanical pressures and compartmental fluid flow on CSD wave characteristics in a setting

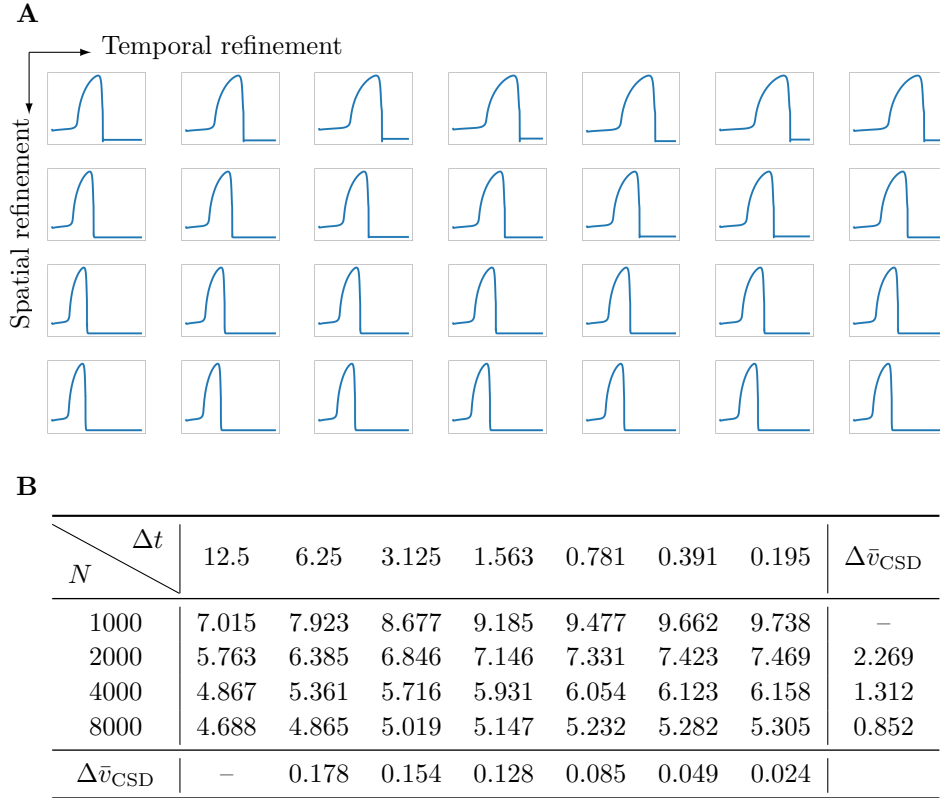
4 *A. J. Ellingsrud, N. Boullé, P. E. Farrell, and M. E. Rognes*

Fig. 1. Wave properties during refinement in space (N) and time (Δt , ms) in a 1D domain of length 10 mm at $t = 50$ s. The PDEs are discretized in time by the previously presented first order scheme from Mori, O’Connell, and Tuttle et al.^{24,28,45} and the ODEs are solved using backward Euler. **A**: Neuron potential $\phi_n(x, 50)$ (mV) versus $x \in \Omega$ (mm). **B**: CSD mean wave speed \bar{v}_{CSD} (mm/min) and difference $\Delta \bar{v}_{\text{CSD}}$ between consecutive refinements.

with two compartments (neurons and ECS). Here, we present a low order finite element scheme and simulation results for the full model in three compartments (neurons, glial and ECS) and study the convergence of the scheme. The scheme again displays optimal convergence rates during refinement in space and time for a problem with smooth manufactured solutions, and meets similar challenges as the zero flow limit model for the CSD case.

The paper is organized as follows. The Mori framework is summarized in Section 2. In Section 3, we present new numerical schemes for the zero flow limit version of the model, along with numerical convergence and performance studies for the suggested schemes in Section 4 and Section 5. The next sections consider the full model. We present a numerical scheme in Section 6 along with numerical convergence studies in Section 7, while in Section 8 we present results from a full model simulation of CSD including microscopic fluid dynamics. Finally, Section 9

contains a discussion and concluding remarks. The code used to obtain the simulation results presented within this work is based on FEniCS²³, and is publicly available⁹.

2. Mathematical model

The tissue of interest is represented as a domain $\Omega \subset \mathbb{R}^d$, with $d \in \{1, 2, 3\}$. Moreover, the tissue is composed of R compartments indexed by $r = 1, \dots, R$. We assume that $r = R$ always denotes the ECS, and that other compartments communicate with the ECS only. Let time $t \in (0, T]$. For a self-contained exposition, we summarize the Mori framework²⁴ below.

2.1. Governing equations

We will consider the following system of coupled, time-dependent, nonlinear partial differential equations. Find the *volume fractions* $\alpha_r : \Omega \times (0, T] \rightarrow [0, 1)$ such that for each $t \in (0, T]$:

$$\frac{\partial \alpha_r}{\partial t} + \nabla \cdot (\alpha_r u_r) = -\gamma_{rR} w_{rR}, \quad \text{for } r = 1, \dots, R-1, \quad (2.1a)$$

$$\frac{\partial \alpha_R}{\partial t} + \nabla \cdot (\alpha_R u_R) = \sum_{r=1}^{R-1} \gamma_{rR} w_{rR}, \quad (2.1b)$$

where $u_r : \Omega \times (0, T] \rightarrow \mathbb{R}^d$ is the *fluid velocity field* of compartment r (m/s). The *transmembrane water flux* w_{rR} between compartment r and the ECS is driven by osmotic and oncotic pressure, and will be discussed further in Section 2.2. The coefficient γ_{rR} (1/m) represents the area of cell membrane between compartment r and the ECS per unit volume of tissue. By definition, the volume fractions sum to 1, and hence:

$$\alpha_R = 1 - \sum_{r=1}^{R-1} \alpha_r. \quad (2.2)$$

where $\alpha_r \geq 0$. Further, for each ion species $k \in K$, find the *ion concentrations* $[k]_r : \Omega \times (0, T] \rightarrow \mathbb{R}$ (mol/m³) and the *electrical potentials* $\phi_r : \Omega \times (0, T] \rightarrow \mathbb{R}$ (V) such that for each $t \in (0, T]$:

$$\frac{\partial(\alpha_r [k]_r)}{\partial t} + \nabla \cdot J_r^k = -\gamma_{rR} J_{rR}^k, \quad r = 1, \dots, R-1, \quad (2.3a)$$

$$\frac{\partial(\alpha_R [k]_R)}{\partial t} + \nabla \cdot J_R^k = \sum_{r=1}^{R-1} \gamma_{rR} J_{rR}^k, \quad (2.3b)$$

where $J_r^k : \Omega \times (0, T] \rightarrow \mathbb{R}^d$ is the *ion flux density* (mol/(m²s)) for each ion species k . Modelling the *transmembrane ion flux density* (mol/(m²s)) J_{rR}^k for each ion species $k \in K$ will be discussed further in Section 2.2. Note that (2.3) follow from first principles and express conservation of ion concentrations for the bulk of each

6 *A. J. Ellingsrud, N. Boullé, P. E. Farrell, and M. E. Rognes*

region. Moreover, we assume that the ion flux densities (and *a fortiori* the ion concentrations and electrical potentials) satisfy:

$$\gamma_{rR} C_{rR} \phi_{rR} = z^0 F a_r + \alpha_r F \sum_k z^k [k]_r, \quad r = 1, \dots, R-1, \quad (2.4a)$$

$$-\sum_r^{R-1} \gamma_{rR} C_{rR} \phi_{rR} = z^0 F a_R + \alpha_R F \sum_k z^k [k]_R, \quad (2.4b)$$

where z^k (dimensionless) is the *valence* of ion species k , a_r (mol/m³) is the *amount of immobile ions*, F (C/mol) denotes *Faraday's constant*, and C_{rR} (F/m²) is the *membrane capacitance* of the membrane between compartment r and the ECS.

In this paper, we assume that the ion flux densities J_r^k can be expressed in terms of the ion concentrations, the electrical potentials, the volume fractions and the fluid velocity field as:

$$J_r^k = -D_r^k \nabla [k]_r - \frac{D_r^k z^k}{\psi} [k]_r \nabla \phi_r + \alpha_r u_r [k]_r, \quad r = 1, \dots, R. \quad (2.5)$$

Here, D_r^k (m²/s) denotes the *effective diffusion coefficient* of ion species k in the region r and may be a given constant or e.g. a spatially varying scalar field dependent of α_r . The constant $\psi = RTF^{-1}$ combines Faraday's constant F , the *absolute temperature* T (K), and the *gas constant* R (J/(K mol)). We assume that the system is isothermal, i.e. T is constant. The ion flux density, i.e. the flow rate of ions per unit area, is thus modelled as the sum of three terms: (i) the diffusive movement of ions due to ionic gradients $-D_r^k \nabla [k]_r$, (ii) the ion concentrations that are transported via electrical potential gradients, i.e. the ion migration $-D_r^k z^k \psi^{-1} [k]_r \nabla \phi_r$ where $D_r^k \psi^{-1}$ is the *electrochemical mobility* and (iii) the convective movement $\alpha_r u_r [k]_r$ of ions.

We now turn to the dynamics of the fluid velocity field u_r and the *mechanical pressure* $p_r : \Omega \times (0, T] \rightarrow \mathbb{R}$ (Pa). Let the compartmental fluid velocity u_r (m/s) be expressed as:

$$u_r = -\kappa_r \left(\nabla \tilde{p}_r + F \sum_k z^k [k]_r \nabla \phi_r \right), \quad \tilde{p}_r = p_r - RT \frac{a_r}{\alpha_r}, \quad r = 1, \dots, R, \quad (2.6)$$

where κ_r (m⁴/(N s)) is the water permeability in compartment r . The fluid velocity field is thus modelled as the sum of three terms: (i) the mechanical pressure gradient $-\kappa_r \nabla p_r$, (ii) the oncotic pressure gradient $\kappa_r \nabla (RT \frac{a_r}{\alpha_r})$, and (iii) the electrostatic forces $-\kappa_r F \sum_k z^k [k]_r \nabla \phi_r$. The mechanical pressure p_r in compartment r and in the ECS p_R may be related as:

$$p_r - p_R = \tau_r(\alpha_r), \quad r = 1, \dots, R-1, \quad (2.7)$$

where the *mechanical tension per unit area of the membrane* $\tau_r = \tau_r(\alpha_r)$ is to be modelled. A simple relation could be $\tau_r = S_r(\alpha_r - \alpha_r^0)$, where S_r (Pa/m³) denotes the stiffness of the membrane between compartment r and the ECS, and α_r^0 is the

volume fraction at which the membrane has no mechanical tension. Furthermore, we assume that the volume-fraction weighted velocity is divergence free, that is:

$$\nabla \cdot \left(\sum_{r=1}^R \alpha_r u_r \right) = 0. \quad (2.8)$$

Upon inserting (2.6)–(2.7) into (2.8), we obtain the following equation for the extracellular mechanical pressure $p_R : \Omega \times (0, T] \rightarrow \mathbb{R}$ (Pa),

$$\nabla \cdot \left(\sum_{r=1}^R \kappa_r \alpha_r \left(-\nabla p_R + \nabla RT \frac{a_r}{\alpha_r} - F \sum_k z^k [k]_r \nabla \phi_r \right) - \sum_{r=1}^{R-1} \kappa_r \alpha_r \nabla \tau_r \right) = 0. \quad (2.9)$$

The combination of (2.1a) and (2.2)–(2.4), together with the insertion of (2.5)–(2.6) and (2.9), defines a system of $|R||K| + 2|R| + 1$ equations for the $|R||K| + 2|R| + 1$ unknown scalar fields. Appropriate initial conditions, boundary conditions, and importantly membrane mechanisms close the system.

2.2. Membrane mechanisms

The transmembrane water flux w_{rR} is driven by a combination of mechanical and osmotic pressure, and can be expressed as:

$$w_{rR} = \eta_r \left(p_r - p_R + RT \left(\frac{a_R}{\alpha_R} + \sum_k [k]_R - \frac{a_r}{\alpha_r} - \sum_k [k]_r \right) \right), \quad (2.10)$$

where η_r ($\text{m}^4/(\text{mol s})$) denotes the *water permeability*. The compartmental and extracellular potentials across the membrane are coupled by defining ϕ_{rR} as the jump in the electrical potential across the membrane between compartment r and the ECS (c.f. (2.4)),

$$\phi_{rR} = \phi_r - \phi_R. \quad (2.11)$$

The transmembrane ion flux J_{rR}^k between compartment r and the ECS of ion species k is subject to modelling, and will typically take the form:

$$J_{rR}^k = a_{rR}^k(\phi_{rR}, [k]_r) + p_{rR}^k(\phi_{rR}, [k]_r, s_1, \dots, s_M). \quad (2.12)$$

Here, a_{rR}^k represents active membrane mechanisms (e.g. ionic pumps) and p_{rR}^k denotes passive membrane mechanisms (e.g. leak or voltage gated ion channels, co-transporters). The passive membrane mechanisms typically depend on (unitless) gating variables $s_m = s_m(\phi_{rR})$ for $m \in 1, \dots, M$ governed by an ODE system of the form:

$$\frac{\partial s_m}{\partial t} = \alpha_m(1 - s_m) - \beta_m s_m, \quad (2.13)$$

where $\alpha_m = \alpha_m(\phi_{rR})$ (1/s) and $\beta_m = \beta_m(\phi_{rR})$ (1/s) are rate coefficients³⁹.

8 *A. J. Ellingsrud, N. Boullé, P. E. Farrell, and M. E. Rognes*

2.3. Boundary conditions

The boundary conditions will strongly depend on the problem of interest. If not otherwise stated, we assume that no ion flux or fluid leaves on the boundary $\partial\Omega$, that is,

$$J_r^k(x, t) = 0 \quad \text{and} \quad u_r(x, t) = 0, \quad \text{on } \partial\Omega, \quad (2.14)$$

for $r = 1, \dots, R$.

2.4. Effective diffusion coefficients

We model the effective diffusion coefficients D_r^k for each ion species $k \in K$ by:

$$D_r^k = \alpha_r \chi_r D^k \quad \text{and} \quad D_R^k = \alpha_R D^k, \quad (2.15)$$

for $r = 1, \dots, R-1$, where D^k (m²/s) denotes the diffusion coefficient in water and χ_r (dimensionless) reflects the cellular *gap junction connectivity*.

2.5. Zero flow limit

We first consider a simplified version of the mathematical model presented in Section 2, where the compartmental fluid velocity u_r for $r = 1, \dots, R$ is assumed to be zero. Thus, the advective terms in (2.1a) and (2.5) vanish and (2.9) is decoupled from the rest of the system. The remaining equations, (2.1a) and (2.2)–(2.4) with the insertion of (2.5), describe the dynamics of the volume fractions α_r , the ion concentrations $[k]_r$ and the electrical potentials ϕ_r , for $r \in \{1, \dots, R\}$ and for each $k \in K$.

3. Numerical schemes for the zero flow limit

Below, we present two numerical schemes for the zero flow limit model based on the finite element method.

3.1. Spatial discretization

To obtain a variational formulation, we multiply (2.1a) and (2.3)–(2.4) with suitable test functions, integrate over the domain Ω , integrate terms with higher order derivatives by parts, and insert the boundary condition (2.14). Below, we let $\langle u, v \rangle = \int_{\Omega} uv \, dx$. Let $S_r \subset L^2(\Omega)$, $V_r^k \subset H^1(\Omega)$, $V_R^k \subset H^1(\Omega)$, $T_r \subset H^1(\Omega)$, and $T_R \subset H^1(\Omega)$ for $r = 1, \dots, R-1$ be spaces of functions for $k = 1, \dots, |K|$. The resulting system reads: find $\alpha_r \in S_r$, $[k]_r \in V_r^k$, $\phi_r \in T_r$ ($r = 1, \dots, R-1$), $[k]_R \in V_R^k$,

and $\phi_R \in T_R$ such that:

$$\left\langle \frac{\partial \alpha_r}{\partial t}, s_r \right\rangle + \gamma_{rR} \langle w_{rR}, s_r \rangle = 0, \quad (3.1a)$$

$$\left\langle \frac{\partial \alpha_r [k]_r}{\partial t}, v_r^k \right\rangle - \langle J_r^k, \nabla v_r^k \rangle + \gamma_{rR} \langle J_{rR}^k, v_r^k \rangle = 0, \quad (3.1b)$$

$$\left\langle \frac{\partial \alpha_R [k]_R}{\partial t}, v_R^k \right\rangle - \langle J_R^k, \nabla v_R^k \rangle - \sum_r \gamma_{rR} \langle J_{rR}^k, v_R^k \rangle = 0, \quad (3.1c)$$

$$\langle \gamma_{rR} C_{rR} \phi_{rR}, t_r \rangle - \langle z^0 F a_r, t_r \rangle - \langle F \alpha_r \sum_k z^k [k]_r, t_r \rangle = 0, \quad (3.1d)$$

$$- \sum_r \langle \gamma_{rR} C_{rR} \phi_{rR}, t_R \rangle - \langle z^0 F a_R, t_R \rangle - \langle F \alpha_R \sum_k z^k [k]_R, t_R \rangle = 0, \quad (3.1e)$$

for all $s_r \in S_r$, $v_r^k \in V_r^k$, $v_R^k \in V_R^k$, $t_r \in T_r$, $t_R \in T_R$. The compartmental ion flux J_r^k is given by (2.5), the transmembrane water flux w_{rR} is given by (2.10), while the extracellular volume fraction α_R is given by (2.2). The transmembrane ion fluxes J_{rR}^k will depend on the membrane mechanisms of interest. Note that in the above formulation, the potentials ϕ_r for $r = 1, \dots, R$ are only determined up to a constant.

Next, we discretize the domain Ω by a simplicial mesh \mathcal{T}_h , where h denotes the mesh size. We introduce separate finite element spaces for approximating the unknown fields in the weak formulation (3.1). Specifically, we approximate the volume fractions α_r using piecewise constants (P_0), and the ion concentrations $[k]_r$, $[k]_R$ and potentials ϕ_r , ϕ_R using continuous piecewise linear polynomials P_1^c defined relative to the mesh \mathcal{T}_h .

3.2. Temporal PDE discretization: BDF2 and CN

We apply a second order Backward Differentiation Formula (BDF2) in time, resulting in the following system: given α_r^n , $[k]_r^n$, and $[k]_R^n$ at time level n and α_r^{n-1} , $[k]_r^{n-1}$, and $[k]_R^{n-1}$ at time level $n-1$, find at time level $n+1$ the volume fractions $\alpha_r \in S_r$, the ion concentrations $[k]_r \in V_r^k$, $[k]_R \in V_R^k$ and the potentials $\phi_r \in T_r$,

10 *A. J. Ellingsrud, N. Boullé, P. E. Farrell, and M. E. Rognes*

$\phi_R \in T_R$ such that:

$$\frac{1}{\Delta t} \langle \alpha_r - \frac{4}{3} \alpha_r^n + \frac{1}{3} \alpha_r^{n-1}, s_r \rangle + \frac{2}{3} \gamma_{rR} \langle w_{rR}, s_r \rangle = 0, \quad (3.2a)$$

$$\begin{aligned} \frac{1}{\Delta t} \langle \alpha_r [k]_r - \frac{4}{3} \alpha_r^n [k]_r^n + \frac{1}{3} \alpha_r^{n-1} [k]_r^{n-1}, v_r^k \rangle - \frac{2}{3} \langle J_r^{k,n}, \nabla v_r^k \rangle \\ + \frac{2}{3} \gamma_{rR} \langle J_{rR}^{k,n}, v_r^k \rangle = 0, \end{aligned} \quad (3.2b)$$

$$\begin{aligned} \frac{1}{\Delta t} \langle \alpha_R [k]_R - \frac{4}{3} \alpha_R^n [k]_R^n + \frac{1}{3} \alpha_R^{n-1} [k]_R^{n-1}, v_R^k \rangle - \frac{2}{3} \langle J_R^{k,n}, \nabla v_R^k \rangle \\ - \frac{2}{3} \sum_r \gamma_{rR} \langle J_{rR}^{k,n}, v_R^k \rangle = 0, \end{aligned} \quad (3.2c)$$

$$\langle \gamma_{rR} C_{rR} \phi_{rR}, t_r \rangle - \langle z^0 F a_r, t_r \rangle - \langle F \alpha_r \sum_k z^k [k]_r, t_r \rangle = 0, \quad (3.2d)$$

$$- \sum_r \langle \gamma_{rR} C_{rR} \phi_{rR}, t_r \rangle - \langle z^0 F a_R, t_R \rangle - \langle F \alpha_R \sum_k z^k [k]_R, t_R \rangle = 0, \quad (3.2e)$$

for all $s_r \in S_r$, $v_r^k \in V_r^k$, $v_R^k \in V_R^k$, $t_r \in T_r$, $t_R \in T_R$. The solutions at time level 1 and 0 are given by a backward Euler step and the initial conditions, respectively. Note that the passive part of the membrane flux $J_{rR}^{k,n}$ is treated implicitly, whereas the active part is treated explicitly, both in the BDF2 and the BE time stepping schemes (see (2.12)).

We will also compare with the following Crank-Nicholson (CN) scheme in time: given α_r^n , $[k]_r^n$, and $[k]_R^n$ at time level n , find at time level $n+1$ the volume fractions $\alpha_r \in S_r$, the ion concentrations $[k]_r \in V_r^k$, $[k]_R \in V_R^k$, and the potentials $\phi_r \in T_r$, $\phi_R \in T_R$, such that

$$\frac{1}{\Delta t} \langle \alpha_r - \alpha_r^n, s_r \rangle + \gamma_{rR} \langle w_{rR}^{n+1/2}, s_r \rangle = 0, \quad (3.3a)$$

$$\frac{1}{\Delta t} \langle \alpha_r [k]_r - \alpha_r^n [k]_r^n, v_r^k \rangle - \langle J_r^{k,n+1/2}, \nabla v_r^k \rangle + \gamma_{rR} \langle J_{rR}^{k,n+1/2}, v_r^k \rangle = 0, \quad (3.3b)$$

$$\frac{1}{\Delta t} \langle \alpha_R [k]_R - \alpha_R^n [k]_R^n, v_R^k \rangle - \langle J_R^{k,n+1/2}, \nabla v_R^k \rangle - \sum_r \gamma_{rR} \langle J_{rR}^{k,n+1/2}, v_R^k \rangle = 0, \quad (3.3c)$$

together with (3.2d) and (3.2e), for all $s_r \in S_r$, $v_r^k \in V_r^k$, $v_R^k \in V_R^k$, $t_r \in T_r$, $t_R \in T_R$. Here, $f^{n+1/2}$ denotes the solution at time level $n+1/2$ and is approximated by $(f^n + f^{n+1})/2$, for $f \in \{w_{rR}, J_{rR}^k, J_r^k\}$.

3.3. Strang splitting scheme

We use a second order Strang splitting scheme where we solve the coupled systems of ODEs and PDEs step-wise in the following manner:

- (1) Insert the previous solution of ϕ_{rR} , $[k]_r$, $[k]_R$ into the system of ODEs (2.13), and solve ODEs for a half timestep $\Delta t/2$;
- (2) Solve the system of PDEs (e.g. (3.2)) with values for the gating variables s_1, s_2, \dots, s_M from step (1) for one time step Δt ;

- (3) Insert solution for ϕ_{rR} , $[k]_r$, $[k]_R$ from step (2) into the system of ODEs (2.13), and solve the ODEs for a half timestep $\Delta t/2$;

and continue steps (1)–(3) until the global end time is reached. We compare the Strang splitting scheme with a first order Godunov scheme; see e.g. Sundnes et al.⁴⁰ for a detailed description the Godunov method..

3.4. ODE solvers

We consider three different schemes for the ODE time-stepping: a fourth order Runge-Kutta (RK4) method, a fourth order explicit singly diagonal implicit Runge-Kutta (ESDIRK4) method or a second order backward Euler (BE) method. The ODEs are solved with the RK4 method unless otherwise stated. See e.g. Langtangen and Linge²² for details.

4. Numerical convergence study: smooth analytical solution

To evaluate the numerical accuracy of the various schemes presented above, we begin by constructing a smooth analytical solution using the method of manufactured solutions³³.

4.1. Problem description

We consider a two-compartment version of the model in the zero flow limit and a neuronal (n , $r = 1$) and an extracellular (e , $r = 2$) compartment. We use $1, 2$ and n, e interchangeably for subscripts of our variables and model parameters. In each compartment, we model the movement of potassium (K^+), sodium (Na^+) and chloride (Cl^-). In the numerical experiments of this test, we consider a one dimensional domain $\Omega = [0, 1]$ uniformly meshed with $N \in \{8, 16, 32, 64, 128\}$ elements. We initially set $\Delta t = 10^{-3}$ s, and then halve the timestep with each spatial refinement. The errors are evaluated at $t = 2 \times 10^{-3}$ s. Further, we assume that the transmembrane ion flux J_{ne}^k depends on the gating variables m , h and g governed by the following ODEs:

$$\frac{\partial m}{\partial t} = \phi_{ne}, \quad \frac{\partial h}{\partial t} = \phi_{ne}, \quad \frac{\partial g}{\partial t} = \phi_{ne}, \quad (4.1)$$

where $\phi_{ne} = \phi_n - \phi_e$ is the membrane potential. The analytical solution to the PDE system is given by:

$$\begin{aligned} \alpha_n &= 0.3 - 0.1 \sin(2\pi x) \exp(-t), \\ [Na^+]_n &= 0.7 + 0.3 \sin(\pi x) \exp(-t), & [Na^+]_e &= 1.0 + 0.6 \sin(\pi x) \exp(-t), \\ [K^+]_n &= 0.3 + 0.3 \sin(\pi x) \exp(-t), & [K^+]_e &= 1.0 + 0.2 \sin(\pi x) \exp(-t), \\ [Cl^-]_n &= 1.0 + 0.6 \sin(\pi x) \exp(-t), & [Cl^-]_e &= 2.0 + 0.8 \sin(\pi x) \exp(-t), \\ \phi_n &= \sin(2\pi x) \exp(-t), & \phi_e &= \sin(2\pi x)(1 + \exp(-t)), \end{aligned} \quad (4.2)$$

12 *A. J. Ellingsrud, N. Boullé, P. E. Farrell, and M. E. Rognes*

and the solution to the system of ODEs (4.1) is

$$m = \cos(t) \cos(\pi x), \quad h = \cos(t) \cos(\pi x), \quad g = \cos(t) \cos(\pi x). \quad (4.3)$$

Parameter values are given in Table 1. Initial and boundary conditions are governed by the exact solutions (4.2).

Parameter	Symbol	Value	Unit	Ref.
Temperature	T	310	K	–
Faraday’s constant	F	96485	C/mol	–
Gas constant	R	8.3144598	J/(mol K)	–
Membr. area-to-volume neuron	γ_{ne}	6.3849×10^5	1/m	19
Membr. capacitance neuron	C_{ne}	7.5×10^{-3}	F/m ²	19
Membr. water permeability neuron	η_{ne}	5.4×10^{-10}	m ⁴ /(mol s)	28
Gap junction connectivity neuron	χ_n	0		24
Diffusion coefficient Na ⁺	D^{Na}	1.33×10^{-9}	m ² /s	17
Diffusion coefficient K ⁺	D^{K}	1.96×10^{-9}	m ² /s	17
Diffusion coefficient Cl ⁺	D^{Cl}	2.03×10^{-9}	m ² /s	17
Valence Na ⁺	z^{Na}	1		–
Valence K ⁺	z^{K}	1		–
Valence Cl [–]	z^{Cl}	–1		–

Table 1. Physical model parameters. We use SI base units, that is, Kelvin (K), Coulomb (C), mole (mol), meter (m), second (s), and Joule (J). The values are collected from Hille et al.¹⁷, Kager et al.¹⁹, Mori²⁴, and O’Connell et al.²⁸. – indicates that a standard value is used.

4.2. Convergence and convergence rates under refinement

Based on the approximation spaces and the time discretization, we expect the optimal theoretical rate of convergence to be 1 in the H^1 -norm and 2 in the L^2 -norm for the concentrations $[k]_n$, $[k]_e$, the potentials ϕ_n , ϕ_e and the gating variables m, h, g , and 1 in the L^2 -norm for the volume fraction α_n . Our numerical observations are in agreement with these optimal rates, both for the BDF2 scheme (Table 2A) and for the CN scheme (Table 2B). We observe second order convergence in the L^2 -norm for the approximation of the extracellular and intracellular concentrations and potentials, and first order convergence in the H^1 -norm. The neuron potential approximated by the CN scheme displays superconvergence between $N = 64$ and $N = 128$ (Table 2B). For the volume fractions, we observe a convergence rate of 1 in the L^2 -norm.

A

N	$\ [\text{Na}]_e - [\text{Na}]_{e_h}\ _{L^2}$	$\ \phi_n - \phi_{n_h}\ _{L^2}$	$\ \alpha_n - \alpha_{n_h}\ _{L^2}$	$\ m - m_h\ _{L^2}$
8	5.74E-03(—)	7.66E-02(—)	1.58E-02(—)	9.99E-03(—)
16	1.45E-03(1.99)	1.90E-02(2.01)	7.97E-03(0.98)	2.50E-03(2.00)
32	3.63E-04(1.99)	4.72E-03(2.01)	4.00E-03(1.00)	6.26E-04(2.00)
64	9.11E-05(2.00)	1.17E-03(2.01)	2.00E-03(1.00)	1.56E-04(2.00)
128	2.28E-05(2.00)	2.93E-04(2.00)	1.00E-03(1.00)	3.91E-05(2.00)
N	$\ [\text{Na}]_e - [\text{Na}]_{e_h}\ _{H^1}$	$\ \phi_n - \phi_{n_h}\ _{H^1}$		
8	1.50E-01(—)	1.02E+00(—)		
16	7.53E-02(1.00)	5.05E-01(1.02)		
32	3.77E-02(1.00)	2.52E-01(1.00)		
64	1.88E-02(1.00)	1.26E-01(1.00)		
128	9.43E-03(1.00)	6.28E-02(1.00)		

B

N	$\ [\text{Na}]_e - [\text{Na}]_{e_h}\ _{L^2}$	$\ \phi_n - \phi_{n_h}\ _{L^2}$	$\ \alpha_n - \alpha_{n_h}\ _{L^2}$	$\ m - m_h\ _{L^2}$
8	2.44E-03(—)	1.32E-01(—)	1.52E-02(—)	4.27E-03(—)
16	6.05E-04(2.01)	3.43E-02(1.94)	7.78E-03(0.97)	1.04E-03(2.03)
32	1.52E-04(2.00)	8.68E-03(1.98)	3.91E-03(0.99)	2.59E-04(2.01)
64	3.83E-05(1.99)	2.17E-03(2.00)	1.96E-03(1.00)	6.46E-05(2.00)
128	9.83E-06(1.96)	6.54E-05(5.05)	9.82E-04(1.00)	1.61E-05(2.00)
N	$\ [\text{Na}]_e - [\text{Na}]_{e_h}\ _{H^1}$	$\ \phi_n - \phi_{n_h}\ _{H^1}$		
8	1.47E-01(—)	1.17E+00(—)		
16	7.38E-02(1.00)	5.21E-01(1.17)		
32	3.70E-02(1.00)	2.50E-01(1.06)		
64	1.85E-02(1.00)	1.24E-01(1.02)		
128	9.30E-03(0.99)	6.17E-02(1.00)		

Table 2. Selected L^2 (upper panel) and H^1 -errors (lower panel) and convergence rates (in parenthesis) for the BDF2 (**A**) and CN (**B**) schemes at time $t = 0.002$ s. The test was run on the unit interval, and we initially let $\Delta t = 1 \times 10^{-3}$ s, and then halve the timestep with each mesh refinement. The spatial discretization consists of N intervals.

5. Numerical convergence study: physiological CSD wave

Next, we consider the simulation of cortical spreading depression with a sharp wave front. This is a more challenging problem, with characteristics quite different from the previous smooth MMS case. We numerically study the effect of splitting scheme, time-discretization of the PDEs, and discretization of the ODEs.

14 *A. J. Ellingsrud, N. Boullé, P. E. Farrell, and M. E. Rognes***5.1. Problem description**

Parameter	Symbol	Value	Unit	Ref.
Na ⁺ leak conductance neuron	$g_{n,\text{leak}}^{\text{Na}}$	0.2	S/m ²	19
K ⁺ leak conductance neuron	$g_{n,\text{leak}}^{\text{K}}$	0.7	S/m ²	19
Cl ⁻ leak conductance neuron	$g_{n,\text{leak}}^{\text{Cl}}$	2.0	S/m ²	28
Maximum pump rate neuron	\bar{I}_n	0.1372	A/m ²	48
Threshold for pump [Na ⁺] _r	m_{Na}	7.7	mol/m ³	48
Threshold for pump [K ⁺] _R	m_{K}	2.0	mol/m ³	48

Table 3. Physical parameters for the neuron membrane mechanisms. We use SI base units, i.e. meter (m), mole (mol), Siemens (S) and ampere (A). The values are collected from Kager et al.¹⁹, O’Connell et al.²⁸, and Yao et al.⁴⁸.

We define a more physiological version of the mathematical model considered in Section 4.1 (two compartments, zero flow limit, and a neuronal (n , $r = 1$) and an extracellular compartment (e , $r = 2$)). In each compartment, we again model the movement of potassium (K⁺), sodium (Na⁺) and chloride (Cl⁻). We consider a 1D domain of length 0.01 m (10 mm), and now apply physiologically relevant neuronal membrane mechanisms as described below, notably including a system of ODEs describing the gating variables of voltage-gated sodium and potassium channels. The domain and the transmembrane ion flux densities are taken from the original Mori study²⁴.

Concretely, the transmembrane ion flux densities J_{ne}^k for $k = \{\text{Na}^+, \text{K}^+, \text{Cl}^-\}$ in (2.3) are modelled as:

$$J_{ne}^{\text{Na}} = \frac{1}{Fz_{\text{Na}}} (I_{n,\text{leak}}^{\text{Na}} + I_{\text{NaP}} + 3I_{n,\text{ATP}} + I_{\text{ex}}^{\text{Na}}), \quad (5.1a)$$

$$J_{ne}^{\text{K}} = \frac{1}{Fz_{\text{K}}} (I_{n,\text{leak}}^{\text{K}} + I_{\text{KDR}} + I_{\text{KA}} - 2I_{n,\text{ATP}} + I_{\text{ex}}^{\text{K}}), \quad (5.1b)$$

$$J_{ne}^{\text{Cl}} = \frac{1}{Fz_{\text{Cl}}} (I_{n,\text{leak}}^{\text{Cl}} + I_{\text{ex}}^{\text{Cl}}), \quad (5.1c)$$

where $I_{n,\text{leak}}^{\text{Na}}$, $I_{n,\text{leak}}^{\text{K}}$, $I_{n,\text{leak}}^{\text{Cl}}$, I_{NaP} , I_{KDR} , I_{KA} , and $I_{n,\text{ATP}}$ denote the sodium leak current, the potassium leak current, the chloride leak current, the persistent sodium current, the potassium delayed rectifier current, the transient potassium current, and the Na/K/ATPase current, respectively. Further, $I_{\text{ex}}^{\text{Na}}$, I_{ex}^{K} , and $I_{\text{ex}}^{\text{Cl}}$ are excitatory fluxes used to trigger a cortical spreading depression wave and whose expressions are given by (5.5) in Section 5.1.1 below. Note that the currents (A/m²) are converted to ion fluxes (mol/(m²s)) by dividing by Faraday’s constant F times the valence z^k .

The leak currents (A/m²) of ion species k over the membrane between compart-

ment r (here with $r = n$) and R are modelled as:

$$I_{r,\text{leak}}^k = g_{r,\text{leak}}^k (\phi_{rR} - E_r^k), \quad E_r^k = \frac{RT}{Fz^k} \ln \left(\frac{[k]_R}{[k]_r} \right), \quad (5.2)$$

where E_k^r (V) denotes the Nernst potential. The values for the neuronal leak conductances $g_{n,\text{leak}}^k$ are listed in Table 3.

The current-voltage relation for the voltage-gated currents I_{NaP} , I_{KDR} and I_{KDR} (A/m^2) are described by the Goldman-Hodgkin-Katz (GHK) current equation:

$$I_{\text{GHK}}^k = g^k m^p h^q \frac{F\mu ([k]_e - [k]_n e^{-\mu})}{1 - e^{-\mu}}.$$

Here, $\mu = F\phi_{ne}/(RT)$ is dimensionless, while g^k (m/s) denotes the product of membrane permeability and conductance. The gating variables m and h describe the proportion of open voltage-gated ion channels, and are governed by the following ODEs:

$$\frac{\partial m}{\partial t} = \alpha_m(\phi_{ne})(1 - m) - \beta_m(\phi_{ne})m, \quad (5.3a)$$

$$\frac{\partial h}{\partial t} = \alpha_h(\phi_{ne})(1 - h) - \beta_h(\phi_{ne})h, \quad (5.3b)$$

where the activation rate functions $\alpha_m : \mathbb{R} \rightarrow \mathbb{R}$ and $\beta_m : \mathbb{R} \rightarrow \mathbb{R}$, and the inactivation rate functions $\alpha_h : \mathbb{R} \rightarrow \mathbb{R}$ and $\beta_h : \mathbb{R} \rightarrow \mathbb{R}$, are specified for each current in Table 4. The initial conditions are given in Table 12A (Supplementary Tables).

Current (A/m^2)	Permeability (m/s)	Gates	Voltage dependent rate constants
I_{NaP}	2.0×10^{-7}	$\text{m}^2 \text{ h}$	$\alpha_m = 1/(6 + 6 \exp(-0.143\phi_{ne} - 5.67))$ $\beta_m = 1/6 - \alpha_m$ $\alpha_h = 5.12 \times 10^{-8} \exp(-0.056\phi_{ne} - 2.94)$ $\beta_h = 1.6 \times 10^{-6}/(1 + \exp(-0.2\phi_{ne} - 8))$
I_{KDR}	1.0×10^{-5}	m	$\alpha_m = 0.016 \frac{-\phi_{ne} - 34.9}{\exp(-0.2\phi_{ne} - 6.98) - 1}$ $\beta_m = 0.25 \exp(-0.025\phi_{ne} - 1.25)$
I_{KA}	2.0×10^{-6}	$\text{m}^2 \text{ h}$	$\alpha_m = 0.02 \frac{-\phi_{ne} - 56.9}{\exp(-0.1\phi_{ne} - 56.9) - 1}$ $\beta_m = 0.0175 \frac{\phi_{ne} + 29.9}{\exp(0.1\phi_{ne} + 29.9) - 1}$ $\alpha_h = 0.016 \exp(-0.05\phi_{ne} - 4.61)$ $\beta_h = 0.5/(\exp(-0.2\phi_{ne} - 11.98) + 1)$

Table 4. Permeability, gates and voltage dependent expressions for the activation rates (α) and the inactivation rates (β) for the persistent sodium current (I_{NaP}), the potassium delayed rectifier current (I_{KDR}) and the transient potassium current (I_{KA}) in the neuron membrane. The values are collected from Kager et al.¹⁹ and Yao et al.⁴⁸.

16 *A. J. Ellingsrud, N. Boullé, P. E. Farrell, and M. E. Rognes*

The Na/K/ATPase pump exchanges 2 potassium ions for 3 sodium ions, and the pump current $I_{r,\text{ATP}}$ (A/m²) over the membrane between compartment r (here with $r = n$) and R is modelled as:

$$I_{r,\text{ATP}} = \frac{\hat{I}_r}{\left(1 + \frac{m_K}{[\text{K}^+]_R}\right)^2 \left(1 + \frac{m_{\text{Na}}}{[\text{Na}^+]_r}\right)^3}, \quad (5.4)$$

where \hat{I}_r is the maximum pump rate, and m_{Na} and m_K denote the sodium and potassium pump threshold, respectively. The values for the neuron pump parameters are listed in Table 3.

5.1.1. Initiation of the CSD wave

Following the original Mori study²⁴, we initiate a CSD wave by adding excitatory fluxes to the transmembrane fluxes defined by (5.1) in the following manner:

$$I_{\text{ex}}^k = G_{\text{ex}}(E_r^k - \phi_{nR}),$$

$$G_{\text{ex}}(x, t) = \begin{cases} G_{\text{max}} \cos^2(\pi x/2L_{\text{ex}}) \sin(\pi t/T_{\text{ex}}) & \text{if } x \leq L_{\text{ex}} \text{ and } t \leq T_{\text{ex}}, \\ 0 & \text{otherwise,} \end{cases} \quad (5.5)$$

for $k = \{\text{Na}^+, \text{K}^+, \text{Cl}^-\}$. We set $L_{\text{ex}} = 2.0 \times 10^{-5}$ m, $T_{\text{ex}} = 2$ s, and $G_{\text{max}} = 5.0$ S/m².

5.2. CSD wave characteristics

The excitatory flux stimulation leads to a wave of neuronal depolarization, ionic concentration changes and neuronal swelling spreading through the tissue domain (Figure 2). We observe a dramatic depolarization of the neuron potential: from -71 mV to -8.7 mV, accompanied by a small drop in the extracellular potential: from 0 to -3.9 mV. This latter drop is known as the DC shift, a key characteristic associated with cortical spreading depression³¹. The neuronal depolarization wave is followed by a complete break-down of the ionic homeostasis: a substantial increase in the concentrations of extracellular potassium, and decreases in extracellular sodium and chloride. In response to the ionic shifts, the neurons swell with an increase in volume fraction of up to 10%, while the extracellular space shrinks correspondingly. We observe that although we have not enforced positivity of α_r explicitly, $\alpha_r \geq 0$ holds throughout our numerical experiments.

Experimental studies typically focus on the speed and duration of the CSD wave. We thus define the following quantities of interest to be studied further quantitatively in terms of numerical convergence.

- The point of $x_{\text{peak},50}$ of peak neuron potential ϕ_n at $t = 50$ s.
- The mean CSD wave speed \bar{v}_{CSD} is computed by the distance between the peak neuronal potential at two points (as long as $\phi_n > -20$ mV) divided by the time elapsed to cover that distance.

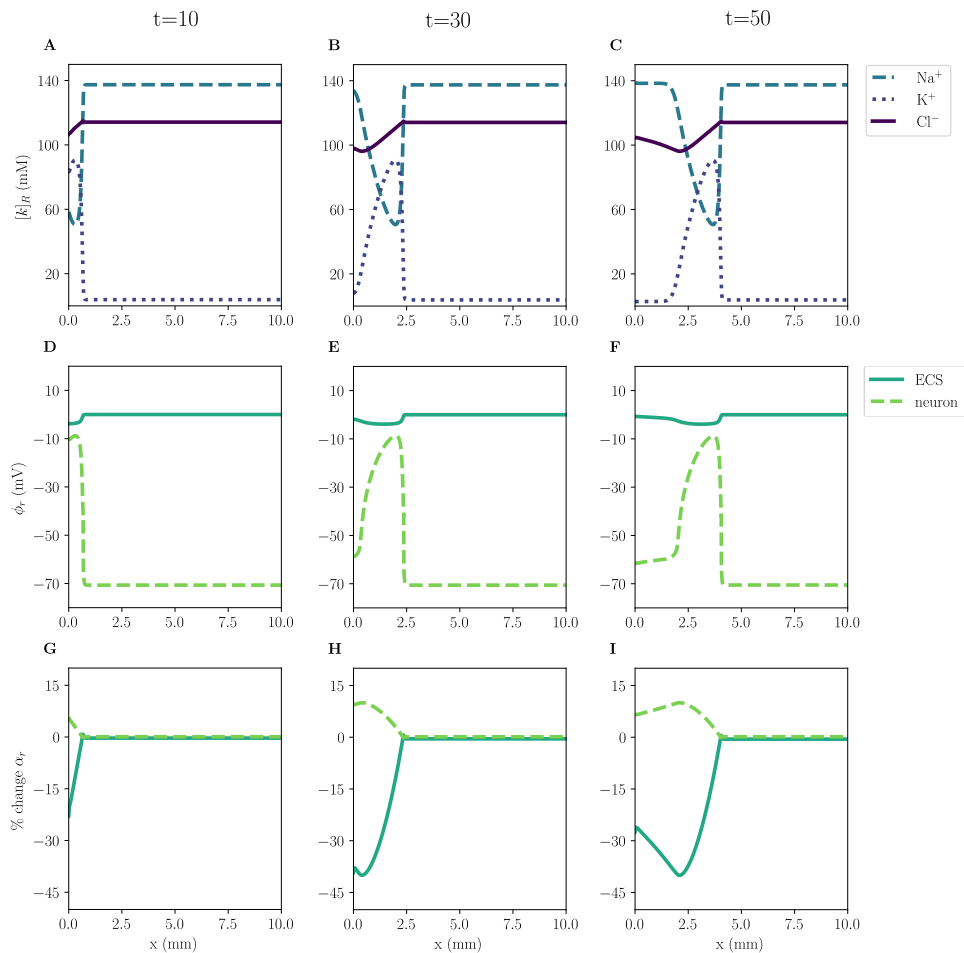


Fig. 2. Snapshot of a CSD wave spreading through the tissue domain – extracellular sodium (Na^+), potassium (K^+) and chloride (Cl^-) concentrations (**A**, **B**, **C**), neuron and extracellular potentials (**D**, **E**, **F**), and neuron and extracellular changes in volume fractions (**G**, **H**, **I**) – at, from left to right, $t = 10, 30, 50$ s. Numerical scheme and resolutions: BDF2, Strang, RK4 with $N = 32000$ and $\Delta t = 0.195$ s.

- The (temporal) duration d_{CSD} of the CSD wave in terms of elevated extracellular potassium levels at $x = 1$ mm, where

$$\mathbb{T} = \{t \mid [\text{K}^+]_R(1, t) > k_{\text{thres}}\}$$

$$d_{\text{CSD}} = \max \mathbb{T} - \min \mathbb{T}$$

with $k_{\text{thres}} = 10$ mM for $t \in (0, T]$.

18 *A. J. Ellingsrud, N. Boullé, P. E. Farrell, and M. E. Rognes*

- The (spatial) width w_{CSD} of the extracellular potassium wave at $t = 50$ s, where

$$\begin{aligned}\mathbb{X} &= \{x \mid [\text{K}^+]_R(x, 50) > k_{\text{thres}}\} \\ w_{\text{CSD}} &= \max \mathbb{X} - \min \mathbb{X}\end{aligned}$$

with $k_{\text{thres}} = 10$ mM for $x \in \Omega$.

5.3. Convergence of the CSD wave characteristics

We begin by considering a reference scheme – based on Strang splitting, a BDF2 method for the PDE time-discretization, and ESDIRK4 for the ODE time-stepping – to compute the mean speed, the (spatial) width, and the (temporal) duration of the CSD wave (cf. Section 5.2) during temporal and spatial refinement, before discussing how variations in terms of splitting scheme, time-stepping and higher order spatial discretization affect accuracy and convergence. Specifically, we apply the reference scheme and calculate the quantities of interest for different mesh resolutions and time steps: $\Delta x_N = 10/N$ mm for $N = 1000, 2000, 4000, 8000, 16000, 32000$ and $\Delta t_i = 12.5/i$ s for $i = 1, 2, 4, 8, 16, 32, 64$. The results are presented in Figure 3. Wave speeds are converted from the native m/s to mm/min for interpretability.

In general, the computed mean wave speed and width increases with decreasing Δt , and decreases with decreasing Δx : the smaller the time step, the faster and wider the wave, while the smaller the mesh size, the slower and narrower the wave (Figure 3A). Regarding the mean wave speed (Figure 3B), we observe that the computed values vary substantially, ranging from 5.063 to 10.090 mm/min. We observe that the spatial errors, estimated by proxy by the difference between consecutive spatial refinements, dominate the temporal errors/differences. In particular, the differences $\Delta \bar{v}_{\text{CSD}}$ in wave speed between the coarsest mesh sizes $N = 1000$ and 2000 are in the range 1.70 – 2.45 mm/min. Conversely, the differences in wave speed between the coarsest time steps $\Delta t = 12.5$ and 6.25 are in the range 0.51 – 0.64 mm/min. For the ultimate spatial and temporal refinement level, we observe a difference of 0.012 and 0.008 mm/min, respectively. Finally, we observe that the wave speed seems to converge in space and time with an estimated wave speed of 5.1 mm/min: the differences $\Delta \bar{v}_{\text{CSD}}$ reduce as Δx and Δt is reduced. There is however no clear rate of convergence.

Similarly, we observe large variations in the computed (spatial) CSD wave width, ranging from 1.121 to 4.420 mm (Figure 3C). The difference (Δw_{CSD}) varies in the range 0.755 – 1.07 mm and 0.062 – 0.280 mm between respectively the coarsest mesh sizes $N = 1000$ and 2000 and the coarsest time steps $\Delta t = 12.5$ and 6.25 s. For the finest time and mesh discretizations, we observe differences of 0.005 mm and 0.002 mm, respectively. Moreover, the differences Δw_{CSD} reduce as the mesh size and time step are reduced. As with the mean wave speed, there is no clear rate of convergence. In contrast, the (temporal) duration d_{CSD} of the CSD wave does not change substantially during refinement in space and time: we observe a duration of elevated extracellular potassium levels of 17 – 18 s for all the spatial

and temporal resolutions considered (results not shown). Finally, we observe that this implicit higher-order (reference) scheme behaves qualitatively similar to the implicit lower-order scheme – based on Godunov splitting, a BE method for the PDE time-discretization, and BE for the ODE time-stepping as shown in Figure 1.

5.4. Choice of discretizations

We turn to evaluate the effect of discretization choices in terms of splitting scheme, time-stepping, and higher order spatial discretization.

Splitting scheme

To evaluate the second order Strang splitting scheme, we compared the computed CSD wave characteristics, peak neuron potentials, and wave speeds with those computed using a first order Godunov splitting scheme (cf. Section 3.3). The computed wave speeds are comparable at given resolutions, and we observe a similar difference decay ($\Delta\bar{v}$) for the Strang and Godunov splitting schemes (see Table 10 in Supplementary Tables).

Time stepping

To assess how the choice of PDE time stepping affects the convergence of the numerical schemes, we repeat the convergence study presented above in Section 5.3 replacing the BDF2 scheme by a Crank-Nicolson (CN) scheme and ESDIRK4 by RK4 for the ODE time stepping (Table 5). We note that choosing an explicit ODE time stepping scheme (RK4) here is based on the observation that CN for the PDE time stepping in combination with implicit ODE time stepping schemes results in a diverging (non-linear) ODE solver.

Importantly, we note that the PDE Newton solver fails to converge for $\Delta t \geq 1.563$ ms for this scheme. Again, we observe that the computed speed and width of the wave decreases with decreasing Δx , and is essentially constant with decreasing Δt (likely due to the already fine timestep required for convergence of the PDE Newton solver). The spatial errors, estimated by proxy by the difference between consecutive spatial refinements, are comparable to those reported for BDF2, and again we obtain an estimated wave speed of 5.1 mm/min for this model scenario.

To assess how the choice of ODE time stepping affects the convergence of the numerical schemes, we repeat the convergence study presented above in Section 5.3 replacing ESDIRK4 by a first-order Backward Euler (BE) scheme or an explicit 4th order Runge-Kutta (RK4) method. For the RK4 method, we observe nearly indistinguishable results as for ESDIRK4 with the important distinction that the RK4 solvers fail to converge for $\Delta t \geq 3.125$ ms (see Supplementary Tables, Table 11A). Also for the BE scheme, the computed wave speed values are similar,

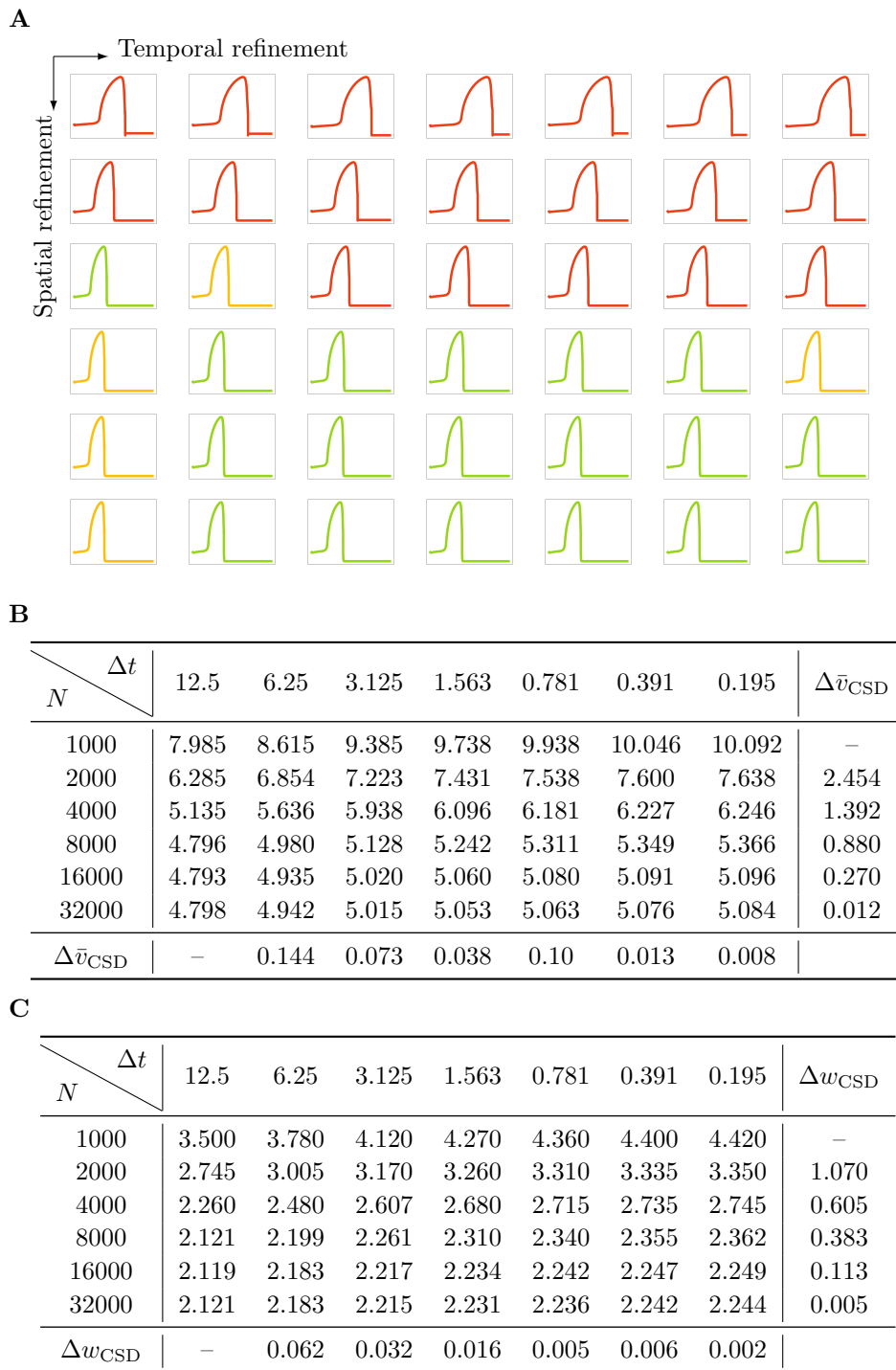
20 *A. J. Ellingsrud, N. Boullé, P. E. Farrell, and M. E. Rognes*

Fig. 3. CSD wave characteristics and quantities of interest under refinement in space (rows) and time (columns). **A**: Neuron potential $\phi_n(x, 50)$ (mV) versus $x \in \Omega$ (mm), where green, yellow, and red represent wave speeds differing by respectively $\pm 5\%$, $\pm 15\%$, and more than $\pm 15\%$ from our estimated wave speed of 5.1 mm/min. **B**: CSD mean wave speed \bar{v}_{CSD} (mm/min) and difference $\Delta \bar{v}_{\text{CSD}}$ between consecutive refinements. **C**: Wave width w_{CSD} (mm) at $t = 50$ s and difference Δw_{CSD} between consecutive refinements. Numerical scheme: Strang splitting, BDF2, ESDIRK4.

A

$N \backslash \Delta t$	12.5	6.25	3.125	1.563	0.781	0.391	0.195	$\Delta \bar{v}_{\text{CSD}}$
1000	*	*	*	*	10.154	10.154	10.154	–
2000	*	*	*	*	7.669	7.669	7.669	2.485
4000	*	*	*	*	6.269	6.269	6.269	1.400
8000	*	*	*	*	5.384	5.386	5.386	0.883
16000	*	*	*	*	5.102	5.103	5.103	0.283
32000	*	*	*	*	5.090	5.090	5.091	0.012
$\Delta \bar{v}_{\text{CSD}}$	–	–	–	–	–	0.000	0.001	

B

$N \backslash \Delta t$	12.5	6.25	3.125	1.563	0.781	0.391	0.195	Δw_{CSD}
1000	*	*	*	*	4.450	4.450	4.450	–
2000	*	*	*	*	3.365	3.365	3.365	1.085
4000	*	*	*	*	2.752	2.755	2.755	0.610
8000	*	*	*	*	2.370	2.371	2.371	0.384
16000	*	*	*	*	2.252	2.252	2.252	0.119
32000	*	*	*	*	2.247	2.247	2.247	0.005
Δw_{CSD}	–	–	–	–	–	0.000	0.000	

Table 5. CSD wave characteristics and quantities of interest under refinement in space (rows) and time (columns). **A**: CSD mean wave speed \bar{v}_{CSD} (mm/min) and difference $\Delta \bar{v}_{\text{CSD}}$ between consecutive refinements. **B**: Wave width w_{CSD} (mm) at $t = 50$ s and difference Δw_{CSD} between consecutive refinements. Numerical scheme: Strang splitting, CN, RK4. * indicates that the solver failed to converge.

but with slightly bigger differences in terms of differences between resolutions (see Supplementary Tables, Table 11B).

Higher order spatial discretization

To assess how the polynomial degree of the finite elements affects the convergence of the numerical schemes, we repeat the convergence study presented in Section 5.3 replacing the lowest order finite element pairings by higher order pairings. We consider the model described in Section 2 discretized with discontinuous piecewise linear polynomials (P_1) for the volume fractions α_r and continuous piecewise linear polynomials of degree 2 (P_2^c) for the ion concentrations and potentials. The finite element software used within this work (FEniCS²³) has automated functionality for solving coupled PDE-ODE systems via the PointIntegralSolver¹² class. The

22 *A. J. Ellingsrud, N. Boullé, P. E. Farrell, and M. E. Rognes*

PointIntegralSolver solves the ODEs at the vertices of the elements and only supports the use of elements with degrees of freedom located at the vertices. Higher order elements are thus not supported. To assess the accuracy and convergence of the higher order scheme, we here consider an alternative implementation where the ODEs are solved at each degree of freedom of the spatial discretization using a backward Euler scheme and a Newton solver.

A

N	$P_0-P_1^c$		$P_1-P_2^c$	
	\bar{v}_{CSD}	$\Delta\bar{v}_{\text{CSD}}$	\bar{v}_{CSD}	$\Delta\bar{v}_{\text{CSD}}$
1000	7.585	–	6.415	–
2000	6.346	1.239	5.416	0.999
4000	5.412	0.934	5.005	0.411
8000	5.005	0.407	4.987	0.018
16000	4.988	0.017	4.989	-0.002
32000	4.989	-0.001	–	–

B

N	$P_0-P_1^c$		$P_1-P_2^c$	
	w_{CSD}	Δw_{CSD}	w_{CSD}	Δw_{CSD}
1000	3.330	–	2.800	–
2000	2.785	0.545	2.380	0.420
4000	2.380	0.405	2.210	0.170
8000	2.210	0.170	2.202	0.008
16000	2.203	0.007	2.203	-0.001
32000	2.203	0.000	–	–

Table 6. Comparison of CSD wave characteristics and quantities of interest under refinement in space between the $P_0-P_1^c$ spatial discretization described in Section 3.1 and a $P_1-P_2^c$ discretization (both solved using the implementation allowing for higher order elements). **A**: CSD mean wave speed \bar{v}_{CSD} (mm/min) and difference $\Delta\bar{v}_{\text{CSD}}$ between consecutive refinements. **B**: Wave width w_{CSD} (mm) at $t = 50$ s and difference Δw_{CSD} between consecutive refinements. Numerical scheme: Strang splitting, BDF2, BE using $\Delta t = 3.125$ ms.

In Table 6, we compare the CSD wave characteristics (wave speed \bar{v}_{CSD} and wave width w_{CSD}) computed after solving the system with the two different spatial discretizations: $P_0-P_1^c$ and $P_1-P_2^c$. The numerical scheme consists of a second order Strang splitting, together with a BDF2 time-stepping scheme for the PDE and a backward Euler (BE) scheme for the system of ODEs, with a timestep of $\Delta t = 3.125$ ms. We observe that the wave speed and wave width computed using a second order $P_1-P_2^c$ spatial discretization with a mesh of N elements (where

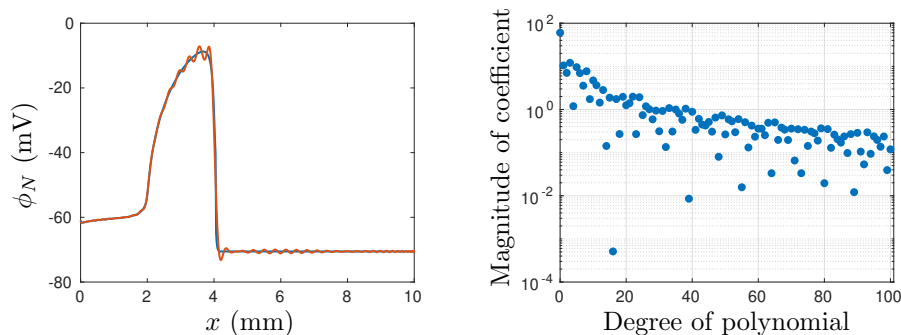


Fig. 4. Left: Neuron potential ϕ_n (blue) together with its polynomial approximation of degree 100 (red) computed using the Chebfun software⁶. Right: Magnitude of the Chebyshev coefficients of the polynomial approximation to ϕ_n .

$N \in \{1000, 2000, 4000, 8000, 16000\}$) are similar to the quantities obtained by a P_0 - P_1^c discretization with $2N$ elements (i.e. the same number of degrees of freedom).

We also study the approximation of the neuron potential by arbitrary higher-order polynomials to compare low-degree finite element spatial discretization against higher order discretizations or global spectral methods¹⁴. First, the system of equations is solved using a P_0 - P_1^c finite element scheme with a large spatial discretization of $N = 32000$. We then use the Chebfun software to approximate the neuron potential with Chebyshev polynomials^{6,13}.

In Figure 4 (left), we display the original function ϕ_n (in blue), together with its polynomial approximation of degree 100 (in red). We see that the approximation has large oscillating errors near the wave front located at $x = 4$ mm, which is likely due to Wilbraham–Gibbs phenomenon⁴². On the right panel of Figure 4, we report the coefficients of the polynomial approximation to ϕ_n of degree 100 constructed by Chebfun. The magnitude of the Chebyshev coefficients seems to decay algebraically at a rate of -1.2 , suggesting that a very large polynomial degree (of order $10^4 - 10^5$) would be required to approximate the solution to (2.1a) and (2.3)–(2.4) accurately.

5.5. Numerical performance for the zero flow limit

So far, we have investigated the convergence of the different schemes via studying key functionals of the solution. To evaluate the performance and scalability of the implementation of the schemes for the model in the zero flow limit, we consider an additional set of experiments measuring the memory usage and CPU timings^a. We evaluate both the standard implementation and the implementation allowing for higher order finite elements. For the standard implementation, we consider simulations with BDF2 and ESDIRK4 time stepping for the PDEs and the ODEs,

^aTimings were performed on a Lenovo ThinkPad 2.70GHz x 4 Intel Core i7-7500U CPU using FEniCS 2019.1.0 without parallelization.

respectively, and compare the performance of Godunov and Strang splitting. For the implementation allowing for higher order finite elements we consider simulations with Strang splitting, BDF2 time PDE stepping, BE time ODE stepping, and compare performance of using P_0 - P_1^c and P_1 - P_2^c elements.

For both the Godunov and Strang splitting schemes and the standard implementation, we observe that the memory usage increases linearly with the number of degrees of freedom: doubling the number of degrees of freedom leads to an increase in memory of a factor 2 (see Table 7A and B). We observe that the CPU time for the simulations grows linearly with the number of degrees of freedom: doubling the number of degrees of freedom leads to an increase in total simulation time of a factor 2. In the Strang splitting scheme, the ODEs are solved twice for each PDE step and we thus expect the total ODE stepping time to be greater than for the Godunov splitting scheme (where the ODEs are only solved once per PDE step). Indeed, the total ODE stepping time is about twice as large for Strang splitting as for Godunov splitting (Table 7). Conversely, the time required for finite element assembly and LU solves is comparable for Godunov splitting and Strang splitting. In total, the simulation time is higher for Strang splitting than Godunov (11 – 18%). Moreover, the total simulation time is dominated by the cost of finite element assembly and LU solves (84% for Godunov splitting, 72% for Strang splitting). Finally, the time required for finite element assembly is comparable to that of the LU solves for both splitting schemes.

The simulation time of the higher order P_1 - P_2^c discretization (with the implementation allowing for higher order schemes) is reported in Table 7D. For a given number of mesh elements $N \in \{4000, 8000, 16000\}$, we compare the timings with the P_0 - P_1^c discretization with a mesh of $2N$ elements (Table 7C) so that the underlying systems have the same number of degrees of freedom as well as approximately the same accuracy, following the linear convergence of the P_1 - P_2^c discretization as observed in Section 5.4. We then see that the total time needed to run the full simulation is approximately 21 – 40% higher for the P_1 - P_2^c discretization. This difference is explained by the higher density of the finite element matrices resulting from the P_1 - P_2^c discretization compared to the choice of P_0 - P_1^c .

In conclusion, Strang and Godunov splitting yield comparable accuracy and memory usage. We observe that Strang splitting yields higher total CPU time than Godunov. When varying (ODE and PDE) time stepping schemes we observe minor variations in terms of accuracy. The higher order element scheme (P_1 - P_2^c) has both a higher total CPU time and memory usage than the lower order spatial scheme (P_0 - P_1), whereas the accuracy is comparable. We find that the accurate computation of CSD wave characteristics (wave speed and wave width) requires a very fine spatial and fine temporal resolution for all schemes tested.

A

N	Dofs	M (MiB)	T_A (s)	T_{LU} (s)	T_{PDE} (s)	T_{ODE} (s)	T_{tot} (s)
8000	72008	117	329	350	679	129	813
16000	144008	199	659	707	1366	258	1632
32000	288008	396	1438	1520	2958	559	3526

B

N	Dofs	M (MiB)	T_A (s)	T_{LU} (s)	T_{PDE} (s)	T_{ODE} (s)	T_{tot} (s)
8000	72008	118	333	352	685	259	954
16000	144008	199	677	719	1396	536	1932
32000	288008	396	1367	1451	2818	1086	3916

C

N	Dofs	M (MiB)	T_A (s)	T_{LU} (s)	T_{PDE} (s)	T_{ODE} (s)	T_{tot} (s)
8000	72008	130	–	–	696	253	953
16000	144008	223	–	–	1411	506	1922
32000	288008	446	–	–	3076	1115	4198

D

N	Dofs	M (MiB)	T_A (s)	T_{LU} (s)	T_{PDE} (s)	T_{ODE} (s)	T_{tot} (s)
4000	72008	165	–	–	1017	309	1331
8000	144008	285	–	–	1693	511	2209
16000	288008	567	–	–	3902	1182	5091

Table 7. CPU timings and memory usage for approximating solutions in the zero flow limit. Dofs: number of degrees of freedom in the linear (PDE) system, M: Maximal memory usage of simulation relative to baseline. T_A : CPU time for finite element assembly, T_{LU} : CPU time for LU solver, T_{ODE} : CPU time for ODE stepping, T_{PDE} : CPU time for PDE stepping (in **A** and **B** this equals the sum of T_A and T_{LU}), T_{tot} : Total CPU time for simulation. T_A and T_{LU} are not reported for **C** and **D**. All simulations have $\Delta t = 3.125$ ms and final time $T = 5$ s (i.e. 1600 timesteps). Results from simulations with the standard implementation with BDF2, ESDIRK4, P_0 - P_1^c , and either **A**: Godunov splitting; or **B**: Strang splitting. Results from simulations with the implementation allowing for higher order elements with BDF2, BE, Strang splitting, and either **C**: P_0 - P_1^c elements; or **D**: P_1 - P_2^c elements.

6. Numerical solution of model including fluid dynamics

The previous schemes and experiments considered only the zero flow limit. Here, we present a numerical scheme for the full mathematical model. The variational formulation (6.1) is obtained by multiplying (2.1)–(2.4) and (2.8) by suitable test functions, integrating over the domain Ω , integrating terms with higher order derivatives by parts, and inserting the boundary conditions (2.14). Further, we use a backward Euler scheme for the PDE time discretization. Let $S_r \subset H^1(\Omega)$, $V_r^k \subset H^1(\Omega)$, $V_R^k \subset H^1(\Omega)$, $T_r \subset H^1(\Omega)$, $T_R \subset H^1(\Omega)$, and $Q \subset H^1(\Omega)$ be spaces of functions for $r = 1, \dots, R-1$ and $k = 1, \dots, |K|$. Given α_r^n , $[k]_r^n$, and $[k]_R^n$ at time level n , at each time level $n+1$ find the volume fractions $\alpha_r \in S_r$, the ion concentrations $[k]_r \in V_r^k$, $[k]_R \in V_R^k$, the potentials $\phi_r \in T_r$, $\phi_R \in T_R$, and the extracellular mechanical pressure $p_R \in Q$ such that:

$$\frac{1}{\Delta t} \langle \alpha_r - \alpha_r^n, s_r \rangle - \langle \alpha_r u_r, \nabla s_r \rangle + \gamma_{rR} \langle w_{rR}, s_r \rangle = 0, \quad (6.1a)$$

$$\frac{1}{\Delta t} \langle \alpha_r [k]_r - \alpha_r^n [k]_r^n, v_r^k \rangle - \langle J_r^k, \nabla v_r^k \rangle + \gamma_{rR} \langle J_{rR}^k, v_r^k \rangle = 0, \quad (6.1b)$$

$$\frac{1}{\Delta t} \langle \alpha_r [k]_R - \alpha_r^n [k]_R^n, v_R^k \rangle - \langle J_R^k, \nabla v_R^k \rangle - \sum_r^{R-1} \gamma_{rR} \langle J_{rR}^k, v_R^k \rangle = 0, \quad (6.1c)$$

$$\langle \gamma_{rR} C_{rR} \phi_{rR}, t_r \rangle - \langle z^0 F a_r, t_r \rangle - \langle F \alpha_r \sum_k z^k [k]_r, t_r \rangle = 0, \quad (6.1d)$$

$$- \sum_r^{R-1} \langle \gamma_{rR} C_{rR} \phi_{rR}, t_R \rangle - \langle z^0 F a_R, t_R \rangle - \langle F \alpha_R \sum_k z^k [k]_R, t_R \rangle = 0, \quad (6.1e)$$

$$- \langle \sum_r^R \alpha_r u_r, \nabla q \rangle = 0, \quad (6.1f)$$

for all $s_r \in S_r$, $v_r^k \in V_r^k$, $v_R^k \in V_R^k$, $t_r \in T_r$, $t_R \in T_R$, $q \in Q$. The compartmental ion flux J_r^k is given by (2.5), the compartmental fluid velocity u_r is given by (2.6), the transmembrane water flux w_{rR} is given by (2.10), while the transmembrane ion fluxes J_{rR}^k are subject to modelling. As before, the potentials ϕ_r for $r = 1, \dots, R$ and the extracellular mechanical pressure p_R are only determined up to a constant. We employ continuous piecewise linear elements for all variables. Note that $\alpha_r \in L^2(\Omega)$ is sufficient for the weak formulation of the zero flow limit model to be well-defined, whereas in the full model, the gradient of α_r appears via the expression for the compartmental fluid velocities u_r in (2.6), thus suggesting $\alpha_r \in H^1(\Omega)$. For the ODE time stepping, we apply an ESDIRK4 scheme and first order Godunov splitting.

7. Numerical convergence study with fluid dynamics: smooth analytical solution

To evaluate the numerical accuracy of the scheme presented above in Section 6, we construct an analytical solution using the method of manufactured solutions³³. We

consider the full model with three compartments, namely a neuronal (n , $r = 1$), a glial (g , $r = 2$) and an extracellular compartment (e , $r = 3$). We use 1, 2, 3 and n, g, e interchangeably for subscripts of our variables and model parameters. In each compartment, we model the movement of potassium (K^+), sodium (Na^+) and chloride (Cl^-). The transmembrane ion fluxes J_{rR}^k are taken to be passive leak fluxes, i.e.:

$$J_{rR}^k = \frac{1}{Fz^k} I_{r,\text{leak}}^k, \quad (7.1)$$

where $I_{r,\text{leak}}^k$ is defined by (5.2) for compartment r and ion species k . The neuronal leak conductances $g_{n,\text{leak}}^k$ are given in Table 3, and the glial leak conductances $g_{g,\text{leak}}^k$ for Na^+ and Cl^- are given in Table 8, whereas the glial K^+ conductance is given by (8.1). We consider a one dimensional domain $\Omega = [0, 1]$ uniformly meshed with $N \in \{8, 16, 32, 64, 128\}$ elements. We initially set $\Delta t = 10^{-3}$ s, and then halve the timestep with each spatial refinement. The errors are evaluated at $t = 2 \times 10^{-3}$ s. The analytical solutions are given by (4.2)–(4.3) for the neuronal and extracellular tissue variables, and by the following for the glial tissue variables and the extracellular mechanical pressure:

$$\begin{aligned} \alpha_g &= 0.2 - 0.1 \sin(2\pi x) \exp(-t), & [Na]_g &= 0.5 + 0.6 \sin(\pi x) \exp(-t), \\ [K]_g &= 0.5 + 0.2 \sin(\pi x) \exp(-t), & [Cl]_g &= 1.0 + 0.8 \sin(\pi x) \exp(-t), \\ \phi_g &= \sin(2\pi x) \exp(-t), & p_R &= \sin(2\pi x) \exp(-t). \end{aligned} \quad (7.2)$$

Parameters values are given in Table 1 and Table 8. Initial and boundary conditions are governed by the exact solutions (4.2) and (7.2).

Based on properties of the approximation spaces and the time discretization, we expect the optimal rate of convergence to be 1 in the H^1 -norm and 2 in the L^2 -norm for the volume fractions $\alpha_n, \alpha_g, \alpha_e$, the ion concentrations $[k]_n, [k]_g, [k]_e$, the potentials ϕ_n, ϕ_g, ϕ_e and the mechanical pressure p_e . Our numerical observations are in agreement with the theoretically optimal rates (Table 9).

8. Numerical convergence study: physiological CSD model with microscopic fluid mechanics

8.1. Problem description

Finally, we consider the full model with a neuronal (n , $r = 1$), glial (g , $r = 2$) and extracellular compartment (e , $r = 3$) and three ion species, namely potassium (K^+), sodium (Na^+) and chloride (Cl^-). Cortical spreading depression is triggered by applying excitatory fluxes to the neurons as described in (5.5) in the one-dimensional domain of length 10 mm. The physiological parameters values are given in Table 1 and Table 8, whereas the initial conditions are given in Table 12B (Supplementary Tables).

The neuronal membrane mechanisms are as described in Section 5.1. For the glial membrane mechanisms we follow O'Connell²⁸ and consider leak currents modelled as in (5.2) (with $r = g$) for sodium (Na^+) and chloride (Cl^-), and a potassium

28 *A. J. Ellingsrud, N. Boullé, P. E. Farrell, and M. E. Rognes*

Parameter	Symbol	Value	Unit	Ref.
Na ⁺ leak conductance glial	$g_{g,\text{leak}}^{\text{Na}}$	0.072	S/m ²	29
Cl ⁻ leak conductance glial	$g_{g,\text{leak}}^{\text{Cl}}$	0.5	S/m ²	29
KIR resting conductance glial	g_{KIR}^0	1.3	S/m ²	38
Maximum NaKCl rate glial	g_{NaKCl}	8.13×10^{-4}	A/m ²	28
Maximum pump rate glial	\hat{I}_g	0.0372	A/m ²	28
Membr. area-to-volume glial	γ_{ge}	6.3849×10^5	1/m	19
Membr. capacitance glial	C_{ge}	7.5×10^{-3}	F/m ²	19
Membr. water permeability glial	η_{ge}	5.4×10^{-10}	m ⁴ /(mol s)	28
Membrane stiffness neuron	S_{ne}	2.85×10^3	Pa/m ³	–
Membrane stiffness glial	S_{ge}	2.85×10^3	Pa/m ³	–
Gap junction connectivity glial	χ_g	0.05		–
Neuronal water permeability	κ_n	0	m ⁴ /(N s)	*
Glial water permeability	κ_g	5.0×10^{-16}	m ⁴ /(N s)	–
ECS water permeability	κ_e	5.0×10^{-16}	m ⁴ /(N s)	–

Table 8. Physical parameters for the glial membrane and mechanical pressure. We use SI base units, that is, meter (m), mole (mol), Siemens (S) and ampere (A). The values are collected from O’Connell et al.²⁸, Østby et al.²⁹, Steinberg et al.³⁸, and Yao et al.⁴⁸. The symbol – indicates that the value is chosen by the authors, as we could not find any relevant values in the literature. * The neuronal water permeability is set to zero as we assume no gap junctions connecting the neurons.

inward rectifier current (I_{KIR} , A/m²). Following Steinberg et al.³⁸, the KIR conductance g_{KIR} (S/m²) is modelled as:

$$g_{\text{KIR}} = g_{\text{KIR}}^0 \sqrt{\frac{[\text{K}^+]_R}{3}} \frac{1 + \exp(\frac{18.5}{42.5})}{1 + \exp(\frac{\phi_{ge} - E_K^g + 18.5}{42.5})} \frac{1 + \exp(\frac{-118.6 - 85.2}{44.1})}{1 + \exp(\frac{-118.6 + \phi_{ge}}{44.1})}, \quad (8.1)$$

where g_{KIR}^0 (S/m²) is the resting membrane conductance, and corresponds to the conductance when $\phi_{ge} = E_K^g$ and $[\text{K}^+]_e = [\text{K}^+]_e^0$. The Na/K/ATPase pump (ATP) occurs in both the neuron and glial membrane, and is modelled as in (5.4). Finally, the current through the NaKCl cotransporter I_{NaKCl} (A/m²) is modelled as:

$$I_{\text{NaKCl}} = g_{\text{NaKCl}} \ln \left(\frac{[\text{Na}^+]_g [\text{K}^+]_g [\text{Cl}^-]_g^2}{[\text{Na}^+]_e [\text{K}^+]_e [\text{Cl}^-]_e^2} \right). \quad (8.2)$$

In summary, the total currents over the glial membrane are modelled by (8.3) (with the currents (A/m²) are converted to ion fluxes (mol/(m²s)) by dividing by

N	$\ [\text{Na}]_e - [\text{Na}]_{e_h}\ _{L^2}$	$\ \phi_n - \phi_{n_h}\ _{L^2}$	$\ \alpha_n - \alpha_{n_h}\ _{L^2}$	$\ p_e - p_{e_h}\ _{L^2}$
8	2.47E-03(2.05)	7.19E-02(1.94)	1.73E-03(2.14)	1.31E+01(3.40)
16	6.11E-04(2.02)	1.81E-02(1.99)	4.13E-04(2.06)	2.26E+00(2.53)
32	1.52E-04(2.00)	4.54E-03(2.00)	1.02E-04(2.02)	4.79E-01(2.24)
64	3.80E-05(2.00)	1.14E-03(2.00)	2.54E-05(2.00)	1.15E-01(2.06)
128	9.51E-06(2.00)	3.15E-04(1.85)	6.35E-06(2.00)	2.41E-02(2.25)
n	$\ [\text{Na}]_e - [\text{Na}]_{e_h}\ _{H^1}$	$\ \phi_n - \phi_{n_h}\ _{H^1}$		
8	1.51E-01(1.00)	1.02E+00(1.01)		
16	7.55E-02(1.00)	5.05E-01(1.02)		
32	3.77E-02(1.00)	2.52E-01(1.01)		
64	1.89E-02(1.00)	1.26E-01(1.00)		
128	9.42E-03(1.00)	6.28E-02(1.00)		

Table 9. Selected L^2 -errors (upper panel) and H^1 -errors (lower panel) and convergence rates (in parenthesis) for the full scheme at time $t = 0.002$ s. The test was run on the unit interval, and we initially let $\Delta t = 0.001$ s, and then half the timestep in each series. The spatial discretization consists of N intervals.

Faraday's constant F times the valence z^k):

$$J_g^{\text{Na}} = \frac{1}{Fz^{\text{Na}}} (I_{g,\text{leak}}^{\text{Na}} + 3I_{g,\text{ATP}} + I_{\text{NaKCl}} + I_{\text{ex}}^{\text{Na}}), \quad (8.3a)$$

$$J_g^{\text{K}} = \frac{1}{Fz^{\text{K}}} (I_{\text{KIR}} - 2I_{g,\text{ATP}} + I_{\text{NaKCl}} + I_{\text{ex}}^{\text{K}}), \quad (8.3b)$$

$$J_g^{\text{Cl}} = \frac{1}{Fz^{\text{Cl}}} (I_{g,\text{leak}}^{\text{Cl}} + 2I_{\text{NaKCl}} + I_{\text{ex}}^{\text{Cl}}). \quad (8.3c)$$

Here, $I_{\text{ex}}^{\text{Na}}$, I_{ex}^{K} , and $I_{\text{ex}}^{\text{Cl}}$ are excitatory fluxes used to trigger a cortical spreading depression wave, see (5.5) in Section 5.1.1.

8.2. CSD wave characteristics

As in the zero flow limit scenario, excitatory flux stimulation leads to a CSD wave traveling through the tissue: we observe neuronal depolarization, neuronal and ECS ionic concentration changes, and neuronal swelling (Figure 5). Moreover, we observe that the glial potential depolarizes: from -81 to -31 mV, accompanied by a small drop in the extracellular potential from 0 to -5 mV. Substantial alterations in the intra- and extracellular ion compositions follow the depolarization wave: we observe an increase in the concentrations of extracellular potassium, and decreases in extracellular sodium and chloride. In response to the ionic shifts, the neurons and glial cells swell with an increase in volume fractions of respectively 12.5% and 6.8%, while the extracellular space shrinks correspondingly. We note that the neural and extracellular dynamics are qualitatively similar to those in the case of two

30 *A. J. Ellingsrud, N. Boullé, P. E. Farrell, and M. E. Rognes*

compartments (neurons, ECS) in the zero flow limit (c.f. Figure 2), which is in accordance with the (numerical) findings reported by O’Connell et al²⁸.

The CSD wave is accompanied by a decrease in the mechanical pressures, from the baseline of 0 kPa down to -288 , -334 and -389 kPa in the neuronal, glial and extracellular compartments, respectively (Figure 5 F). The pressure gradients (mechanical and osmotic) drive microscopic fluid flow within the glial and the extracellular compartments. We observe flow rates of up to 1.1 and -0.03 $\mu\text{m/s}$ in the glial and extracellular compartments, respectively; i.e. fluid flows in opposite directions (Figure 6 B,C). During glial swelling, water moves across the glial membrane from the ECS into the glial cells. In response, water within the glial cell network will be pushed away from this area. Indeed, we observe a positive flow rate to the right of the swelling, and a negative flow rate left of the swelling in the glial cells and vice versa in the ECS. We observe no flow in the neuronal compartment, which is expected as the neuronal water permeability is set to zero (Figure 6A).

Next, we (quantitatively) evaluate the numerical convergence of the full model scheme presented in Section 6. To this end, we consider the quantities of interest defined in Section 5.2 in addition to the (spatial) width $w_{\text{CSD,p}}$ of the extracellular mechanical pressure wave at $t = 50$ s, given by

$$\begin{aligned} \mathbb{X} &= \{x \mid p_R(x, 50) > p_{\text{thres}}\} \\ w_{\text{CSD,p}} &= \max \mathbb{X} - \min \mathbb{X} \end{aligned}$$

with $p_{\text{thres}} = -10$ kPa.

8.3. Convergence of CSD wave characteristics during refinement

Drawing on the findings in Section 6, here, we consider the implicit lower-order scheme based on Godunov splitting, a BE method for the PDE time-discretization, and ESDIRK4 for the ODE time-stepping – to compute the mean speed (cf. Section 5.2) and the (spatial) width of the extracellular mechanical pressure wave (cf. Section 8.2) for different mesh resolutions and time steps: $\Delta x_N = 10/N$ mm for $N = 1000, 2000, 4000, 8000, 16000, 32000$ and $\Delta t_i = 12.5/i$ s for $i = 1, 2, 4, 8, 16, 32, 64$. The results are presented in Figure 7. Wave speeds are converted from the native m/s to mm/min for interpretability.

As in the zero flow limit, the computed mean wave speed and the extracellular mechanical pressure wave width increases with decreasing Δt , and decreases with decreasing Δx : the smaller the time step, the faster and wider the wave, while the smaller the mesh size, the slower and narrower the wave (Figure 7A–C). The behavior of the mean wave speed is qualitatively similar to that in the schemes for the zero flow limit (cf. 1). The computed extracellular mechanical pressure wave width vary substantially, ranging from 2.409 to 4.67 mm.

The differences $\Delta w_{\text{CSD,p}}$ in the extracellular mechanical pressure wave width between the coarsest mesh sizes $N = 1000$ and 2000 are in the range $2.96 - 4.67$ mm, while $\Delta w_{\text{CSD,p}}$ between the coarsest time steps $\Delta t = 12.5$ and 6.25 are in the

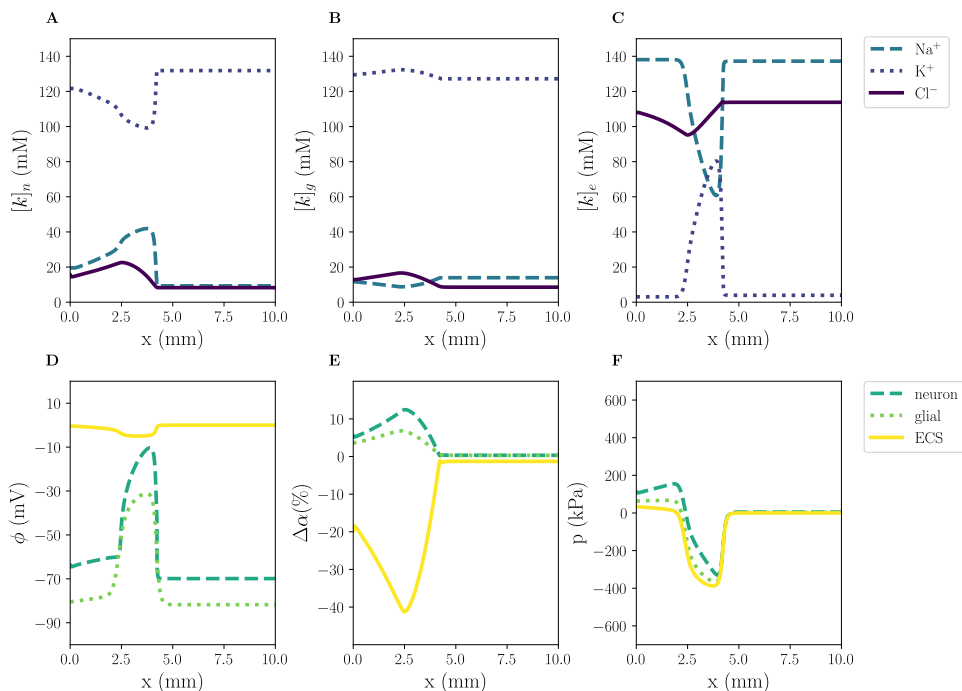


Fig. 5. Full model simulation of a CSD wave. Snapshots at $t = 50$ s of neuronal, glial and extracellular ion concentrations (A, B, C), electrical potentials (D), change in volume fractions (E) and mechanical pressure (F).

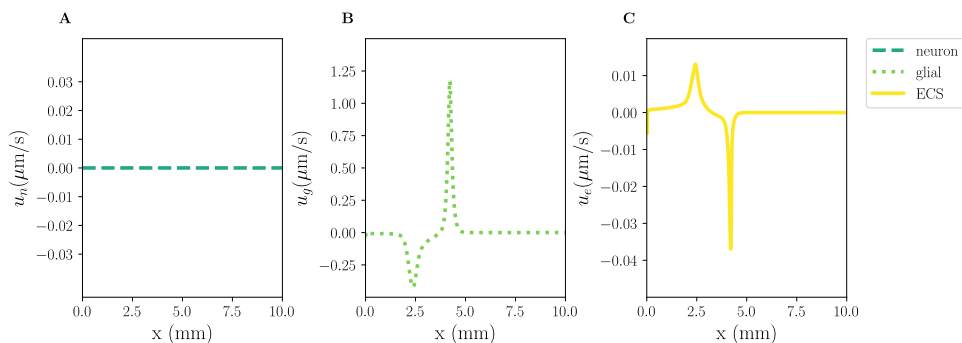


Fig. 6. Full model simulation of a CSD wave: fluid velocities. Snapshots at $t = 50$ s of compartmental fluid velocities in the neurons (A), the glial cells (B), and the ECS (C).

range 2.409 – 3.910 mm. For the finest time and mesh resolutions, we observe that $\Delta w_{\text{CSD},p} = 0.005$ and 0.344 mm, respectively; thus the spatial error continues to dominate. Finally, we observe that $\Delta w_{\text{CSD},p}$ decreases as we refine the discretizations in time and space. There is however no clear convergence rate (Figure 7A, B).

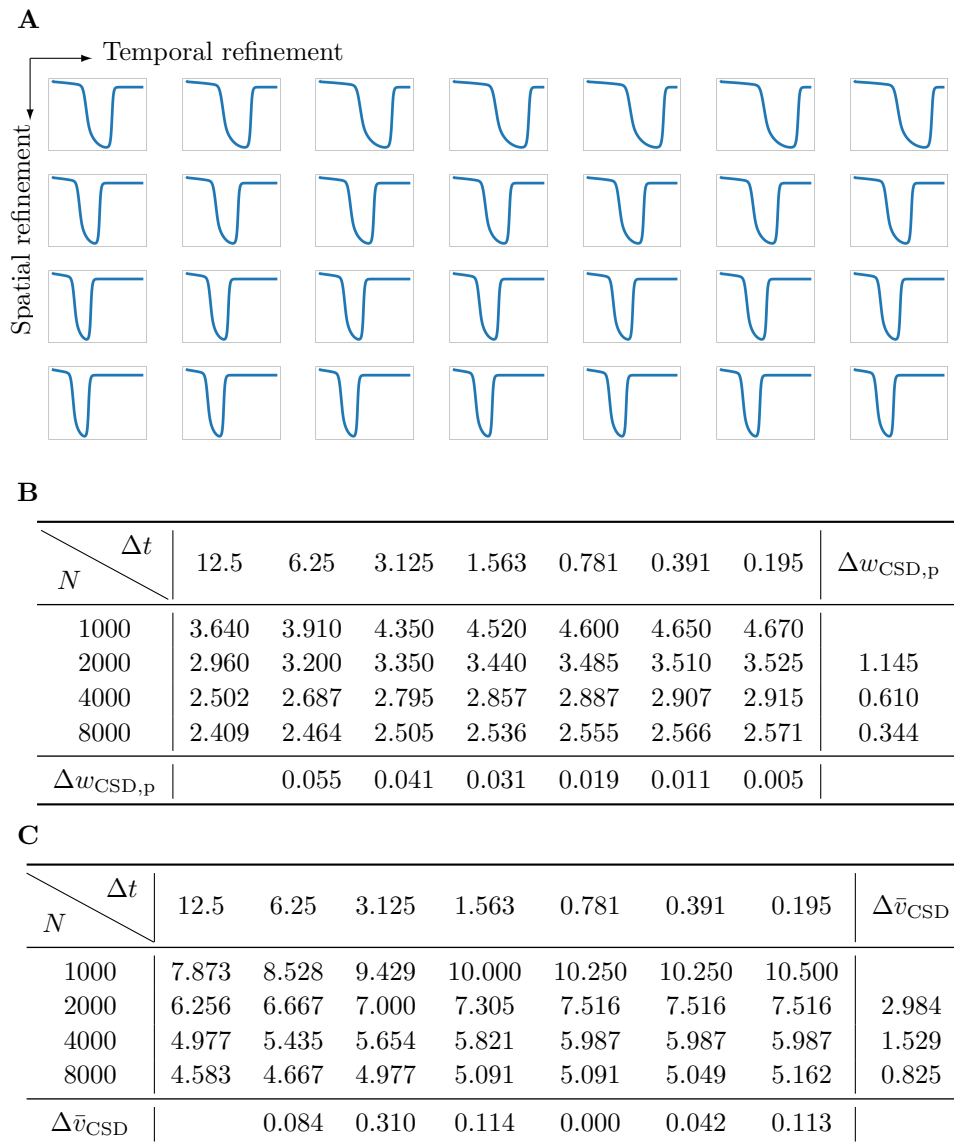
32 *A. J. Ellingsrud, N. Boullé, P. E. Farrell, and M. E. Rognes*

Fig. 7. Full model simulation: CSD wave properties during refinement in space (N) and time (Δt , ms) in a 1D domain of length 10 mm at $t = 50$ s. **A**: Extracellular mechanical pressure $p_R(x, 50)$ (kPa) versus $x \in \Omega$ (mm). **B**: Extracellular mechanical pressure wave width (mm) and difference $\Delta w_{\text{CSD},p}$ between consecutive refinements. **C**: CSD mean wave speed \bar{v}_{CSD} (mm/min) and difference $\Delta \bar{v}_{\text{CSD}}$ between consecutive refinements.

9. Discussion and concluding remarks

We have presented and analyzed finite element-based splitting schemes for a mathematical framework modelling ionic electrodiffusion and water movement in biological tissue in general, and brain tissue in particular. We have evaluated the schemes in terms of their numerical properties, including accuracy, convergence, and computational efficiency, for idealized scenarios as well as for challenging, physiologically realistic problem settings.

The schemes display optimal convergence rates in space for problems with smooth manufactured solutions. However, the physiological CSD setting is challenging: we find that the accurate computation of CSD wave characteristics (wave speed and wave width) requires a very fine spatial and fine temporal resolution for all schemes tested. Indeed, different splitting and time stepping schemes and lower and higher order finite element schemes give comparable results in terms of accuracy. Overall, the error associated with the spatial discretization dominates. Explicit PDE and/or ODE time stepping schemes easily fail to converge even for only moderately coarse time steps, but yield accurate results for very fine timesteps. In light of the long time scale associated with CSD (seconds to minutes), the small time steps imposed by the explicit schemes (less than a millisecond) represent a severe restriction.

The mathematical framework studied here was presented by Mori in 2015²⁴, and has been used to simulate cortical spreading depression in a three-compartment setting (including neurons, glial cells and extracellular space)²⁸, and in multiple spatial dimensions⁴⁵. However, little has been reported on numerical properties of discretizations of this model. The aforementioned studies^{28,45} have used time steps of the order 10 ms and mesh sizes of the order 0.156–0.02 mm (corresponding to $N = 64 - 500$ cf. Figure 1). Our findings indicate that high resolution is required to accurately compute CSD wave properties and that low-to-moderate resolutions can substantially overestimate (or, but more rarely, underestimate) the CSD wave speed. We expect our finite element findings to extend also to comparable finite difference or finite volume discretizations.

In terms of limitations, we have here compared different numerical schemes in terms of accuracy, with less emphasis on computational complexity or cost. We consider these numerical investigations as a starting point and guide for future theoretical studies. Another research direction would be the extension of this study to the two-dimensional CSD model studied by O’Connell²⁷ and Tuttle⁴⁴, where the development of multigrid solvers seems crucial to reach the high spatial resolution needed to obtain accurate solutions.

This paper focuses on numerical challenges related to approximating systems for ionic electrodiffusion and microscopic water movement. We remark that the full model simulation, including extracellular mechanical pressure, yields pressure differences far greater than what one might expect in this setting (~ 6 times atmospheric pressure). It seems natural to reevaluate whether the current compartmental fluid

34 *A. J. Ellingsrud, N. Boullé, P. E. Farrell, and M. E. Rognes*

velocity model best represents the physiology, in particular the fluid velocity component driven by electrostatic forces. On the other hand, it is well-established that large osmotic pressure gradients indeed are present in the brain environment.

In conclusion, our findings show that numerical simulation of ionic electrodiffusion and water movement in brain tissue is feasible, but requires care numerically and substantial computational resources. Numerical schemes or solution approaches that retain accuracy at a lower computational expense would enable the study of a wide array of phenomena in brain physiology, including in the context of pathological conditions.

Appendix A. Supplementary Tables

$N \backslash \Delta t$	12.5	6.25	3.125	1.563	0.781	0.391	0.195	$\Delta \bar{v}_{\text{CSD}}$
1000	8.000	8.631	9.385	9.738	9.938	10.046	10.092	–
2000	6.262	6.862	7.223	7.431	7.538	7.600	7.638	2.454
4000	5.138	5.636	5.938	6.096	6.181	6.227	6.246	1.392
8000	4.798	4.978	5.128	5.242	5.311	5.349	5.366	0.880
$\Delta \bar{v}_{\text{CSD}}$	–	0.180	0.150	0.114	0.069	0.038	0.017	

Table 10. CSD mean wave speed \bar{v}_{CSD} (mm/min) and difference in CSD mean wave speed $\Delta \bar{v}_{\text{CSD}}$ between consecutive refinements in space (rows) and time (columns). Numerical scheme: Godunov splitting, BDF2, ESDIRK4.

A

$N \backslash \Delta t$	12.5	6.25	3.125	1.563	0.781	0.391	0.195	$\Delta \bar{v}_{\text{CSD}}$
1000	*	*	*	*	9.938	10.046	10.092	–
2000	*	*	*	*	7.538	7.600	7.638	2.454
4000	*	*	*	*	6.181	6.227	6.246	1.392
8000	*	*	*	*	5.311	5.349	5.366	0.880
$\Delta \bar{v}_{\text{CSD}}$	–	–	–	–	–	0.038	0.017	

B

$N \backslash \Delta t$	12.5	6.25	3.125	1.563	0.781	0.391	0.195	$\Delta \bar{v}_{\text{CSD}}$
1000	7.323	8.338	9.077	9.554	9.831	9.985	10.062	–
2000	5.938	6.608	7.054	7.338	7.492	7.585	7.623	2.439
4000	4.970	5.487	5.835	6.038	6.150	6.212	6.238	1.385
8000	4.727	4.922	5.080	5.212	5.293	5.339	5.361	0.877
$\Delta \bar{v}_{\text{CSD}}$	–	0.195	0.158	0.132	0.081	0.046	0.022	

Table 11. CSD mean wave speed \bar{v}_{CSD} (mm/min) and difference in CSD mean wave speed $\Delta \bar{v}_{\text{CSD}}$ between consecutive refinements in space (rows) and time (columns). Numerical scheme: Strang, BDF2, and RK4 (**A**) or BE (**B**). * indicates that the solver failed to converge.

36 *A. J. Ellingsrud, N. Boullé, P. E. Farrell, and M. E. Rognes***A**

Parameter	Symbol	Value	Unit
neuron volume fraction	α_n^0	0.8	
Na ⁺ concentration neuron	$[\text{Na}]_n^0$	9.3	mol/m ³
K ⁺ concentration neuron	$[\text{K}]_n^0$	132	mol/m ³
Cl ⁻ concentration neuron	$[\text{Cl}]_n^0$	8.0	mol/m ³
Na ⁺ concentration ECS	$[\text{Na}]_e^0$	137	mol/m ³
K ⁺ concentration ECS	$[\text{K}]_e^0$	4	mol/m ³
Cl ⁻ concentration ECS	$[\text{Cl}]_e^0$	114	mol/m ³
potential neuron	ϕ_n^0	-0.070	V
potential ECS	ϕ_e^0	0.0	V

B

Parameter	Symbol	Value	Unit
neuron volume fraction	α_n^0	0.5	
glial volume fraction	α_g^0	0.3	
Na ⁺ concentration neuron	$[\text{Na}]_n^0$	9.3	mol/m ³
K ⁺ concentration neuron	$[\text{K}]_n^0$	132	mol/m ³
Cl ⁻ concentration neuron	$[\text{Cl}]_n^0$	8.0	mol/m ³
Na ⁺ concentration glial	$[\text{Na}]_g^0$	13	mol/m ³
K ⁺ concentration glial	$[\text{K}]_g^0$	128	mol/m ³
Cl ⁻ concentration glial	$[\text{Cl}]_g^0$	8.0	mol/m ³
Na ⁺ concentration ECS	$[\text{Na}]_e^0$	137	mol/m ³
K ⁺ concentration ECS	$[\text{K}]_e^0$	4	mol/m ³
Cl ⁻ concentration ECS	$[\text{Cl}]_e^0$	114	mol/m ³
potential neuron	ϕ_n^0	-0.070	V
potential glial	ϕ_g^0	-0.082	V
potential ECS	ϕ_e^0	0.0	V
mechanical pressure ECS	p_e^0	0.0	V

Table 12. Initial values for state variables in the zero flow limit (**A**) and in the full model (**B**). We use SI base units; that is, meter (m), and mole (mol).

Acknowledgments

The authors thank Didrik Bakke Dukefoss, Rune Enger, Geir Halmes, Erlend A. Nagelhus, and Klas Pettersen for valuable and constructive discussions on cortical spreading depression and brain electrophysiology.

AJE and MER have received support the European Research Council (ERC) under the European Union’s Horizon 2020 research and innovation programme under grant agreement 714892. PEF acknowledges support from the Engineering and Physical Sciences Research Council (grants EP/R029423/1 and EP/V001493/1). NB acknowledges support from the Engineering and Physical Sciences Research Council Centre for Doctoral Training in Industrially Focused Mathematical Modelling (grant EP/L015803/1) in collaboration with Simula Research Laboratory.

References

1. P. Aitken and G. Somjen, The sources of extracellular potassium accumulation in the CA1 region of hippocampal slices, *Brain Res.* **369** (1986) 163–167.
2. F. Brocard, N. A. Shevtsova, M. Bouhadfane, S. Tazerart, U. Heinemann, I. A. Rybak and L. Vinay, Activity-dependent changes in extracellular Ca²⁺ and K⁺ reveal pacemakers in the spinal locomotor-related network, *Neuron* **77** (2013) 1047–1054.
3. A. C. Charles and S. M. Baca, Cortical spreading depression and migraine, *Nat. Rev. Neurol.* **9** (2013) 637.
4. J. R. Cressman, G. Ullah, J. Ziburkus, S. J. Schiff and E. Barreto, The influence of sodium and potassium dynamics on excitability, seizures, and the stability of persistent states: I. Single neuron dynamics, *J. Comput. Neurosci.* **26** (2009) 159–170.
5. F. Ding, J. O’Donnell, Q. Xu, N. Kang, N. Goldman and M. Nedergaard, Changes in the composition of brain interstitial ions control the sleep-wake cycle, *Science* **352** (2016) 550–555.
6. T. A. Driscoll, N. Hale and L. N. Trefethen, *Chebfun Guide* (Pafnuty Publications, 2014).
7. R. Eisenberg, V. Barcilon and R. Mathias, Electrical properties of spherical syncytia, *Biophys. J.* **25** (1979) 151–180.
8. R. S. Eisenberg and E. A. Johnson, Three-dimensional electrical field problems in physiology, *Prog. Biophys. Mol. Biol.* **20** (1970) 1–65.
9. A. J. Ellingsrud and N. Boullé, Supplementary code: Accurate numerical simulation of electrodiffusion and osmotic water movement in brain tissue, <https://bitbucket.org/adaje/supplementary-code-accurate-numerical-simulation-of/src/master/>, 2020.
10. A. J. Ellingsrud, A. Solbrå, G. T. Einevoll, G. Halmes and M. E. Rognes, Finite element simulation of ionic electrodiffusion in cellular geometries, *Front. Neuroinform.* **14** (2020) 11.
11. R. Enger, D. B. Dukefoss, W. Tang, K. H. Pettersen, D. M. Bjørnstad, P. J. Helm, V. Jensen, R. Sprengel, K. Vervaeke, O. P. Ottersen et al., Deletion of aquaporin-4 curtails extracellular glutamate elevation in cortical spreading depression in awake mice, *Cereb. Cortex* **27** (2017) 24–33.
12. P. E. Farrell, J. E. Hake, S. W. Funke and M. E. Rognes, Automated adjoints of coupled PDE-ODE systems, *SIAM J. Sci. Comput.* **41** (2019) C219–C244.
13. M. S. Floater and K. Hormann, Barycentric rational interpolation with no poles and high rates of approximation, *Numer. Math.* **107** (2007) 315–331.

38 *A. J. Ellingsrud, N. Boullé, P. E. Farrell, and M. E. Rognes*

14. D. Gottlieb and S. A. Orszag, *Numerical analysis of spectral methods: theory and applications* (SIAM, 1977).
15. G. Halmes, T. Mäki-Marttunen, D. Keller, K. H. Pettersen, O. A. Andreassen and G. T. Einevoll, Effect of ionic diffusion on extracellular potentials in neural tissue, *PLoS Comput. Biol.* **12** (2016) e1005193.
16. L. Hertz, Possible role of neuroglia: a potassium-mediated neuronal–neuroglial–neuronal impulse transmission system, *Nature* **206** (1965) 1091–1094.
17. B. Hille et al., *Ion channels of excitable membranes*, volume 507 (Sinauer Sunderland, MA, 2001).
18. N. Hübel and M. A. Dahlem, Dynamics from seconds to hours in Hodgkin–Huxley model with time-dependent ion concentrations and buffer reservoirs, *PLoS Comput. Biol.* **10**.
19. H. Kager, W. J. Wadman and G. G. Somjen, Simulated seizures and spreading depression in a neuron model incorporating interstitial space and ion concentrations, *J. Neurophysiol.* **84** (2000) 495–512.
20. R. Köhling and J. Wolfart, Potassium channels in epilepsy, *Cold Spring Harb. Perspect. Med.* **6** (2016) a022871.
21. S. Kuffler, J. Nicholls and R. Orkand, Physiological properties of glial cells in the central nervous system of amphibia., *J. Neurophysiol.* **29** (1966) 768–787.
22. H. P. Langtangen and S. Linge, *Finite difference computing with PDEs: a modern software approach* (Springer Nature, 2017).
23. A. Logg, K.-A. Mardal and G. Wells, *Automated solution of differential equations by the finite element method: The FEniCS book*, volume 84 (Springer Science & Business Media, 2012).
24. Y. Mori, A multidomain model for ionic electrodiffusion and osmosis with an application to cortical spreading depression, *Physica D* **308** (2015) 94–108.
25. C. Nicholson, G. Ten Bruggencate, H. Stockle and R. Steinberg, Calcium and potassium changes in extracellular microenvironment of cat cerebellar cortex, *J. Neurophysiol.* **41** (1978) 1026–1039.
26. W. Noh, G. Choi, S. Pak, S. Yang and S. Yang, Transient potassium channels: Therapeutic targets for brain disorders, *Front. Cell. Neurosci.* **13** (2019) 265.
27. R. O’Connell, A computational study of cortical spreading depression, Ph.D. thesis, University of Minnesota, 2016.
28. R. O’Connell and Y. Mori, Effects of glia in a triphasic continuum model of cortical spreading depression, *Bull. Math. Biol.* **78** (2016) 1943–1967.
29. I. Østby, L. Øyehaug, G. T. Einevoll, E. A. Nagelhus, E. Plahte, T. Zeuthen, C. M. Lloyd, O. P. Ottersen and S. W. Omholt, Astrocytic mechanisms explaining neural-activity-induced shrinkage of extraneuronal space, *PLoS Comput. Biol.* **5** (2009) e1000272.
30. L. Øyehaug, I. Østby, C. M. Lloyd, S. W. Omholt and G. T. Einevoll, Dependence of spontaneous neuronal firing and depolarisation block on astroglial membrane transport mechanisms, *J. Comput. Neurosci.* **32** (2012) 147–165.
31. D. Pietrobon and M. A. Moskowitz, Chaos and commotion in the wake of cortical spreading depression and spreading depolarizations, *Nat. Rev. Neurosci.* **15** (2014) 379–393.
32. J. Pods, J. Schönke and P. Bastian, Electrodiffusion models of neurons and extracellular space using the Poisson-Nernst-Planck equations — numerical simulation of the intra- and extracellular potential for an axon model, *Biophys. J.* **105** (2013) 242–254.
33. P. J. Roache, *Verification and validation in computational science and engineering* (Hermosa, 1998).

34. M. J. Sætra, G. T. Einevoll and G. Haldnes, An electrodiffusive, ion conserving Pinsky-Rinzel model with homeostatic mechanisms, *PLoS Comput. Biol.* **16** (2020) e1007661.
35. G. Somjen, H. Kager and W. Wadman, Computer simulations of neuron-glia interactions mediated by ion flux, *J. Comput. Neurosci.* **25** (2008) 349–365.
36. R. Srivastava, M. Aslam, S. R. Kalluri, L. Schirmer, D. Buck, B. Tackenberg, V. Rothhammer, A. Chan, R. Gold, A. Berthele et al., Potassium channel KIR4. 1 as an immune target in multiple sclerosis, *N. Eng. J. Med.* **367** (2012) 115–123.
37. C. Staehr, R. Rajanathan and V. V. Matchkov, Involvement of the Na⁺, K⁺-ATPase isoforms in control of cerebral perfusion, *Exp. Physiol.* **104** (2019) 1023–1028.
38. B. Steinberg, Y. Wang, H. Huang and R. Miura, Spatial buffering mechanism: Mathematical model and computer simulations, *Math. Biosci. Eng* **2** (2005) 675–702.
39. D. Sterratt, B. Graham, A. Gillies and D. Willshaw, *Principles of computational modelling in neuroscience* (Cambridge University Press, 2011).
40. J. Sundnes, G. T. Lines, X. Cai, B. F. Nielsen, K.-A. Mardal and A. Tveito, Solving systems of ODEs, in *Computing the Electrical Activity in the Heart* (Springer, 2006), pp. 149–173.
41. X. Tong, Y. Ao, G. C. Faas, S. E. Nwaobi, J. Xu, M. D. Haustein, M. A. Anderson, I. Mody, M. L. Olsen, M. V. Sofroniew et al., Astrocyte Kir4. 1 ion channel deficits contribute to neuronal dysfunction in Huntington’s disease model mice, *Nat. Neurosci.* **17** (2014) 694.
42. L. N. Trefethen, *Approximation Theory and Approximation Practice*, volume 164 of *Other Titles in Applied Mathematics* (SIAM, 2019).
43. L. Tung, A bi-domain model for describing ischemic myocardial D-C potentials., Ph.D. thesis, Massachusetts Institute of Technology, 1978.
44. A. Tuttle, Modeling Regional Variation of Cortical Spreading Depression: A Computational Study, Ph.D. thesis, University of Minnesota, 2019.
45. A. Tuttle, J. R. Diaz and Y. Mori, A computational study on the role of glutamate and NMDA receptors on cortical spreading depression using a multidomain electrodiffusion model, *PLoS Comput. Biol.* **15**.
46. G. Ullah, J. R. Cressman Jr, E. Barreto and S. J. Schiff, The influence of sodium and potassium dynamics on excitability, seizures, and the stability of persistent states: II. Network and glial dynamics, *J. Comput. Neurosci.* **26** (2009) 171–183.
47. D. Uetzschneider, J. Kocsis and M. Devor, Mutual excitation among dorsal root ganglion neurons in the rat, *Neurosci. Lett.* **146** (1992) 53–56.
48. W. Yao, H. Huang and R. M. Miura, A continuum neuronal model for the instigation and propagation of cortical spreading depression, *Bull. Math. Biol.* **73** (2011) 2773–2790.